



Chinese Pharmaceutical Association
Institute of Materia Medica, Chinese Academy of Medical Sciences

Acta Pharmaceutica Sinica B

www.elsevier.com/locate/apsb
www.sciencedirect.com



ORIGINAL ARTICLE

An antibiotic-free platform for eliminating persistent *Helicobacter pylori* infection without disrupting gut microbiota



Yongkang Lai^{a,c,†}, Tinglin Zhang^{b,d,†}, Xiaojing Yin^{a,†}, Chunping Zhu^c,
Yiqi Du^{a,b,d,e,*}, Zhaoshen Li^{a,b,c,d,e,*}, Jie Gao^{b,d,e,*}

^aDepartment of Gastroenterology, Shanghai Changhai Hospital, Naval Medical University, Shanghai 200433, China

^bChanghai Clinical Research Unit, Shanghai Changhai Hospital, Naval Medical University, Shanghai 200433, China

^cDepartment of Gastroenterology, Ganzhou People's Hospital Affiliated to Nanchang University, Ganzhou 341000, China

^dNational Key Laboratory of Immunity and Inflammation, Naval Medical University, Shanghai 200433, China

^eShanghai Key Laboratory of Nautical Medicine and Translation of Drugs and Medical Devices, Shanghai 200433, China

Received 25 December 2023; received in revised form 18 February 2024; accepted 20 February 2024

KEY WORDS

Helicobacter pylori infection;
Antibiotic-free;
Biofilms;
Autophagy;
Gastric mucosal repair;
Drug resistance;
Intestinal microbiota;
Anti-inflammation

Abstract *Helicobacter pylori* (*H. pylori*) infection remains the leading cause of gastric adenocarcinoma, and its eradication primarily relies on the prolonged and intensive use of two antibiotics. However, antibiotic resistance has become a compelling health issue, leading to *H. pylori* eradication treatment failure worldwide. Additionally, the powerlessness of antibiotics against biofilms, as well as intracellular *H. pylori* and the long-term damage of antibiotics to the intestinal microbiota, have also created an urgent demand for antibiotic-free approaches. Herein, we describe an antibiotic-free, multifunctional copper-organic framework (HKUST-1) platform encased in a lipid layer comprising phosphatidic acid (PA), rhamnolipid (RHL), and cholesterol (CHOL), enveloped in chitosan (CS), and loaded in an ascorbyl palmitate (AP) hydrogel: AP@CS@Lip@HKUST-1. This platform targets inflammatory sites where *H. pylori* aggregates through electrostatic attraction. Then, hydrolysis by matrix metalloproteinases (MMPs) releases CS-encased nanoparticles, disrupting bacterial urease activity and membrane integrity. Additionally, RHL disperses biofilms, while PA promotes lysosomal acidification and activates host autophagy,

*Corresponding authors.

E-mail addresses: duyiqi@hotmail.com (Yiqi Du), zhsl@vip.163.com (Zhaoshen Li), gaojiehighclea@smmu.edu.cn (Jie Gao).

†These authors made equal contributions to this work.

Peer review under the responsibility of Chinese Pharmaceutical Association and Institute of Materia Medica, Chinese Academy of Medical Sciences.

<https://doi.org/10.1016/j.apsb.2024.03.014>

2211-3835 © 2024 The Authors. Published by Elsevier B.V. on behalf of Chinese Pharmaceutical Association and Institute of Materia Medica, Chinese Academy of Medical Sciences. This is an open access article under the CC BY-NC-ND license (<http://creativecommons.org/licenses/by-nc-nd/4.0/>).

enabling clearance of intracellular *H. pylori*. Furthermore, AP@CS@Lip@HKUST-1 alleviates inflammation and enhances mucosal repair through delayed Cu²⁺ release while preserving the intestinal microbiota. Collectively, this platform presents an advanced therapeutic strategy for eradicating persistent *H. pylori* infection without inducing drug resistance.

© 2024 The Authors. Published by Elsevier B.V. on behalf of Chinese Pharmaceutical Association and Institute of Materia Medica, Chinese Academy of Medical Sciences. This is an open access article under the CC BY-NC-ND license (<http://creativecommons.org/licenses/by-nc-nd/4.0/>).

1. Introduction

Helicobacter pylori (*H. pylori*) is a well-studied gram-negative bacterium that persistently colonizes the gastric mucosa of approximately half of the global population¹⁻⁴, causing numerous gastrointestinal (GI) and related diseases, including chronic gastritis, peptic ulcer disease, gastric malignancies, and autoimmune diseases⁵⁻⁹. Early in 1994, *H. pylori* was recognized as a Class I carcinogen, and its role in gastric cancer (GC) development was subsequently well established¹⁰⁻¹⁶, which our group identified *H. pylori* as an independent risk factor and predictor of GC risk in a national multicenter study¹⁴. *H. pylori* infection was subsequently shown to serve as the primary and most controllable risk factor for GC prevention¹², which was confirmed through several large-scale multicenter long-term follow-up studies¹⁷⁻²¹. However, despite the obvious benefits and decades of therapeutic testing, eradication of *H. pylori* remains remarkably difficult^{22,23}. Recent epidemiological work by our group^{1,5} indicated that *H. pylori* continues to pose a highly infectious threat to gastric health and has family cluster infections, primarily due to the ineffectiveness and overuse of antibiotics, which instead lead to increasing drug resistance^{23,24}. Thus, improving the efficacy of *H. pylori* treatment without inducing drug resistance poses a long-standing challenge.

Through its long coevolution with humans, *H. pylori* has evolved numerous strategies for evasion and manipulation of host immunity, including invading gastric epithelial cells and producing intracellular protective niches to escape cell and antibiotic killing, as well as forming bacterial biofilms^{23,25,26}. These evasion mechanisms, especially biofilm formation and interconversion between planktonic and sessile states, also significantly limit antibiotic efficacy^{23,27,28} while promoting horizontal gene transfer and overexpression of drug resistance-related efflux pumps^{23,29-31}, ultimately resulting in persistent infection in humans. In addition, the limitations and well-known adverse effects of antibiotic overuse, such as altering the intestinal microbiota, have made *H. pylori* eradication extraordinarily difficult. Therefore, new so-called antibiotic-free strategies based on nanoparticles are urgently needed.

HKUST-1 is a copper-based metal-organic framework (MOF) nanoparticle that can be used for the slow release of Cu²⁺ to reduce the cytotoxicity of Cu²⁺ in different applications, including antibacterial and mucosal repair effects^{32,33}. HKUST-1 nanoparticles can be modified to improve their function in different physiological contexts. For instance, rhamnolipid (RHL), an anionic surfactant glycolipid produced by *Pseudomonas* or *Burkholderia* species³⁴, can disrupt biofilm formation, such as that of *H. pylori*, by binding with metal ions in the extracellular polymeric substance (EPS) matrix and blocking the signaling required

for EPS biosynthesis^{30,35}. Modifying the HKUST-1 surface with RHL could, therefore, potentially improve its access to sequestered bacterial cells. Similarly, given its well-established role in numerous cellular physiological processes^{36,37}, especially in promoting calcium ion (Ca²⁺) efflux, phosphatidic acid (PA) could be used with HKUST-1 to induce lysosomal acidification, consequently enhancing autophagic flux^{38,39}. Since autophagy can mediate the clearance of intracellular bacteria through lysosomal degradation²⁵, we hypothesized that PA could help to eliminate *H. pylori* by inducing autophagy. Chitosan (CS) is the N-deacetylation product of chitin and has high biocompatibility and broad-spectrum bactericidal ability^{40,41}. Especially in the low pH environment of the stomach, CS carries more cations due to the protonation of amino groups (NH³⁺), and these polycations interact with the bacterial outer membrane structure, leading to impaired bacterial outer structure, function, and permeability, leakage of bacterial inner components, and eventual death^{9,42}. Furthermore, its positive surface charge allows CS to adsorb to bacteria, including *H. pylori*^{43,44}. Ascorbyl palmitate (AP) is a negatively charged antioxidant that can form a hydrogel that targets positively charged inflammatory sites and is subsequently hydrolyzed by secreted matrix metalloproteinases (MMPs, collagenase IV) that are enriched at the site of inflammation^{45,46}. These advances in biomaterials led us to consider a multifunctional, nonantibiotic platform for eliminating *H. pylori* infection.

Herein, we designed and tested an AP hydrogel loaded with a CS- and lipid-coated Cu-MOF, AP@CS@Lip@HKUST-1, to clear planktonic, intracellular, and biofilm-sequestered *H. pylori* based on the previously reported properties of each component mentioned above. Here, HKUST-1 was first utilized for the eradication of *H. pylori*, and its modification of CS and liposomes could further retard the release of Cu²⁺. In addition to serving as the main source of antibacterial activity, Cu²⁺ (in low concentrations) serves as an essential metal in proteins needed for angiogenesis and collagen deposition in tissue regeneration^{32,47-49}, which will promote the repair of the gastric mucosa and may prevent reinvasion of *H. pylori* after its eradication. We found that AP@CS@Lip@HKUST-1 indeed confers the properties of each component, targeting inflammatory sites with *H. pylori* aggregates and then releasing CS@Lip@HKUST-1, which adheres to the electrostatic attraction between CS and *H. pylori* and kills *H. pylori* by disrupting membrane integrity and blocking urease activity. Importantly, delivery of RHL through this platform effectively disrupted biofilms, while the PA component induced clearance of intracellular *H. pylori*. Finally, we observed that gastric mucosa repair was enhanced, while inflammation decreased with increasingly delayed Cu²⁺ release without disrupting the resident microbiota composition. To our knowledge, this antibiotic-free platform is the first antibiotic-free study that

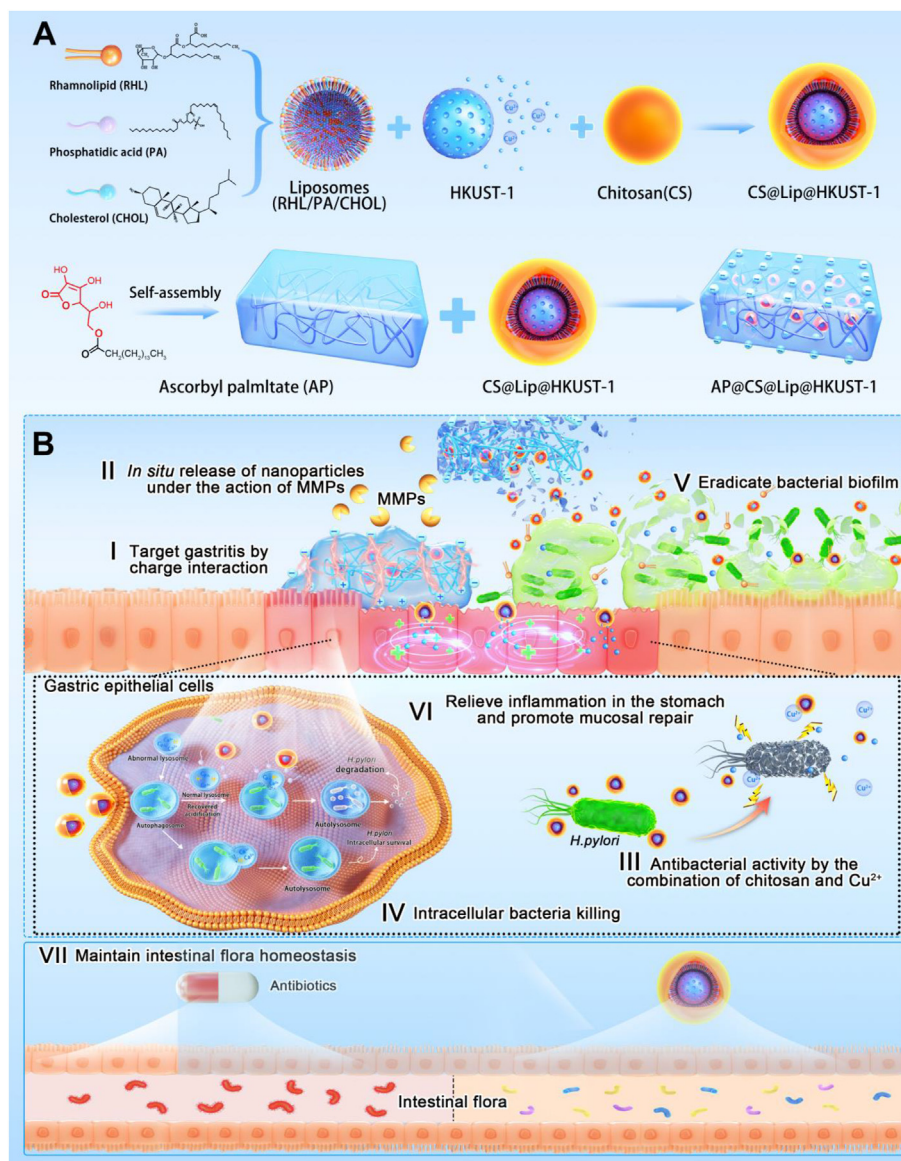
could eradicate *H. pylori* with planktonic, intracellular, and biofilm forms while also promoting gastric mucosal repair without disrupting intestinal flora homeostasis (Scheme 1).

2. Materials and methods

2.1. Materials

Copper acetate monohydrate ($\text{Cu}(\text{CH}_3\text{COO})_2 \cdot \text{H}_2\text{O}$, C105400), trimesic acid ($\text{C}_6\text{H}_3(\text{COOH})_3$, T109692), L-rhamnose monohydrate ($\text{C}_6\text{H}_{12}\text{O}_5 \cdot \text{H}_2\text{O}$, R108982), L- α -phosphatidic acid (egg, chicken, sodium salt, L130341), chitosan ($\text{C}_6\text{H}_{11}\text{NO}_4$)_n, deacetylation degree $\geq 95\%$, viscosity 100–200 mPa s, C105799), L-ascorbic acid 6-palmitate ($\text{C}_{22}\text{H}_{38}\text{O}_7$, A104524), dimethyl sulfoxide ($\text{C}_2\text{H}_6\text{SO}$,

D103281), cholesterol ($\text{C}_{27}\text{H}_{46}\text{O}$, C8667), and gentamicin (G1914) were purchased from Aladdin Bio-Chem Technology Co., Ltd. (Shanghai, China). Clarithromycin (C9490), trimethoprim lactate (T9170), vancomycin (V8050), amphotericin B (A8251), and polymyxin B sulfate (P8350) were obtained from Sigma–Aldrich (Shanghai, China). Cell Counting Kit-8 (40203ES), Live/Dead Cell Staining Kit (40747ES76), and Hieff UNICON® Universal Blue qPCR SYBR Green Master Mix (11184ES08) were purchased from Yeasen Biotechnology (Shanghai, China) Co., Ltd. Urease activity kit was purchased from Solarbio Technology Co. (Beijing, China). The rapid urease test kit was purchased from Shandong Bomed Biotechnology Co. The SYTO 9/PI Live/Dead Bacterial Double Stain Kit (MX4234-40T) was purchased from Shanghai Moukang Biotechnology Co. (Shanghai, China). The Bradford Protein Assay Kit (23246) and TRIzol™ (15596026) were purchased from



Scheme 1 An antibiotic-free biomaterial based on AP@CS@Lip@HKUST-1 as a multifunctional anti-*H. Pylori* platform. A) Schematic illustration of the preparation of CS@Lip@HKUST-1 and AP@CS@Lip@HKUST-1. B) AP@CS@Lip@HKUST-1 exerts a multifunctional antibacterial process by charge interaction (I), releasing nanoparticles *in situ* under the action of MMPs (II), showing antibacterial activity by the combination of copper ions and chitosan (III), eradicating biofilms (IV), promoting autophagy to eradicate intracellular bacteria (V), relieving inflammation in the stomach and restoring gastric mucosa. Meanwhile, AP@CS@Lip@HKUST-1 showed no effect on the intestinal microbiota.

Thermo Fisher Scientific Inc. (Massachusetts, USA). *H. pylori* and gastric epithelial cells (HFE145) were provided by the Department of Gastroenterology, The First Affiliated Hospital of Nanchang University.

2.2. Synthesis of biomaterials

2.2.1. Synthesis of HKUST-1 nanoparticles

HKUST-1 nanoparticles were prepared with slight modification based on a previously reported method⁵⁰. In brief, a solution of 1.2 g $\text{Cu}(\text{CH}_3\text{COO})_2 \cdot \text{H}_2\text{O}$ (6 mmol) and 2.4 g of polyvinylpyrrolidone (PVP) in 60 mL of a 25% aqueous solution of dimethylformamide (DMF) was prepared to obtain the $\text{Cu}(\text{CH}_3\text{COO})_2$ solution. A solution of 0.42 g H_3BTC (trimesic acid, two mmol) in 40 mL of a 25% (v/v) solution of DMF in ethanol was prepared to obtain the H_3BTC solution. The $\text{Cu}(\text{CH}_3\text{COO})_2$ solution was added dropwise to the H_3BTC solution with stirring, and 1 mL of TEA (triethylamine) was added to the reaction mixture. The reaction mixture was stirred for 3 h and sonicated for 30 min to obtain the HKUST-1 suspension. The sample was then washed with ultrapure water, DMF, DCM (dichloromethane), and EtOH (ethanol) three times. Finally, the sample was dispersed in EtOH, and the EtOH was removed by rotary evaporation to obtain HKUST-1 nanoparticles.

2.2.2. Synthesis of Lip@HKUST-1

A solution containing 14 mg/mL RHL, 10 mg/mL PA, and 4 mg/mL CHOL was prepared. Subsequently, 1 mL of each solution was mixed and sonicated for 10 min to obtain the Lip mixed solution (mass ratio of RHL: PA: Chol = 7:5:2). The liposome film was obtained using the lipid thin film method and Lip@HKUST-1 nanoparticles were obtained by adding 1 mL 80 $\mu\text{g}/\text{mL}$ HKUST-1 suspension and then extruded through a nanoextruder (with a filter membrane aperture of 400 nm).

2.2.3. Synthesis of CS@Lip@HKUST-1

CS was dissolved in a 0.2% w/v solution of HAc (acetic acid) in water. Then, 4 mL of CS solution was mixed with 4 mL of the Lip@HKUST-1 suspension and sonicated for 10 min. The mixture was ultrafiltered and centrifuged to remove excess HAc. Subsequently, the sample was extruded using a nanoextruder to obtain CS@Lip@HKUST-1 nanoparticles.

2.2.4. Synthesis of AP@CS@Lip@HKUST-1

The synthesis of the AP hydrogel was performed according to a previous report⁵⁹. In detail, 25 mg of AP was dispersed in 1 mL of DMSO and stirred at 80 °C in a constant-temperature water bath until complete dissolution. Then, 4 mL of CS@Lip@HKUST-1 solution was slowly added dropwise and stirred at a constant temperature for 10 min. AP@CS@Lip@HKUST-1 was obtained by allowing the mixture to stand and cool at room temperature.

2.3. Characterization

The diameter and zeta potential of the nanoparticles were measured using a ZetaSizer Nano-ZS 90 (Malvern Instrument, Malvern, UK). X-ray diffraction (XRD) was performed using a Bruker D2 Phaser (Germany) to observe the crystal structure of the samples. X-ray photoelectron spectroscopy (XPS) was conducted using a Thermo Fisher Scientific K-Alpha (USA) to K-Alpha (USA) to analyze the valence state of the elements. Fourier transform infrared (FTIR) analysis was performed using

a Thermo Fisher Scientific Nicolet iS20 (USA) to identify the chemical structure of the samples. The morphological characteristics and elemental mapping images of the nanoparticles were observed using transmission electron microscopy (TEM) (FEI Talos F200X G2, USA, 200 kV). Scanning electron microscopy (SEM) images were obtained using a field emission scanning electron microscope (ZEISS Sigma 300, Germany). The content of RHL in liposomes was determined by liquid chromatography-mass spectrometry (LC-MS) (Thermo Fisher Scientific Ultimate 3000 UHPLC-Q Exactive, Waltham, Massachusetts, USA) as reported in previous literature⁵¹.

2.4. Cell culture, *H. pylori* strains, and mice

Normal gastric mucosal epithelial cells were obtained from Professor Chuan Xie at the First Affiliated Hospital of Nanchang University and cultured in DMEM/F12 (Gibco, CA, USA) supplemented with 10% FBS and 1% penicillin/streptomycin in a CO_2 incubator (5% CO_2 , 37 °C). The *H. pylori* strains CagA + ATCC43504, TN2GF4, and PMSS1 were used in this study and were also provided by Professor Chuan Xie at the First Affiliated Hospital of Nanchang University. *H. pylori* strains stored at -80 °C were revived on blood agar plates containing 5% sheep blood and 1% mixed antibiotics (10 $\mu\text{g}/\text{mL}$ vancomycin, 5 $\mu\text{g}/\text{mL}$ trimethoprim-treated lactate, 5 $\mu\text{g}/\text{mL}$ cefsulodin sodium, and 5 $\mu\text{g}/\text{mL}$ polymyxin B sulfate). After two generations of incubation, the bacteria were used for the experiments. The liquid culture system for *H. pylori* consisted of Brucella broth, 10% FBS, and 0.5% mixed antibiotics, and the cultures were incubated on a microshaker.

All animal procedures in this study were approved by the Ethics Committee of the First Affiliated Hospital of Naval Medical University (Shanghai, China, Approval Number: CHFC(A.E) 2023-017). Specific pathogen-free (SPF) male C57BL/6 mice (5–6 weeks old, body weight 15–25 g) were purchased from Jiangsu GemPharmatech LLC (Nanjing, China) and kept at the SPF level in the Institute of Pancreatic Diseases, Shanghai Changhai Hospital (Shanghai, China). The mice were housed in a room with a temperature of 18–22 °C, a 12-h light–dark cycle, and a relative humidity of approximately 55%.

2.5. Collagenase degradation experiments on AP hydrogels

The degradation rate of AP@CS@Lip@HKUST-1 in different environments was determined using a weighing method similar to that used in a previous study⁵². Briefly, 100 mg of AP@CS@Lip@HKUST-1 was prepared according to the aforementioned method and incubated with 2 mL of PBS (pH 7.4, 37 °C), 2 mL of collagenase IV solution (1, 0.25, 0.0625 and 0.015625 mg/mL) or 2 mL of simulated gastric fluid (SGF) in a dialysis bag (molecular weight cutoff 3500). The samples were placed in a shaker at 100 rpm and 37 °C. At certain time points, samples were taken, lyophilized, and weighed. The degradation rate was calculated using the following Eq. (1):

$$\text{Degradation rate (\%)} = (W_0 - W_t) / W_0 \times 100 \quad (1)$$

where W_0 represents the weight after lyophilization of AP@CS@Lip@HKUST-1 before the experiment, and W_t represents the weight after lyophilization of the samples in the dialysis bag at a certain time interval. In addition, we obtained optical images of the AP hydrogels at different times.

2.6. Release of Cu^{2+} in HKUST-1

The release of Cu^{2+} from HKUST-1 and CS@Lip@HKUST-1 in simulated gastric fluid (SGF, pH 1.5, 37 °C) was assessed with slight modification according to a previous study⁶³. HKUST-1 (80 $\mu\text{g}/\text{mL}$, 5 mL) and CS@Lip@HKUST-1 (80 $\mu\text{g}/\text{mL}$, with HKUST-1 as the concentration reference, 5 mL) were added to a dialysis bag (molecular weight cutoff, MWCO: 3500) and incubated in 20 mL of SGF with continuous shaking (100 rpm, 37 °C). At designated time points, 1 mL of the release medium was collected for Cu^{2+} release analysis using inductively coupled plasma–mass spectrometry (ICP–MS). An equal volume of fresh medium was replenished at 37 °C.

2.7. Cell compatibility and live/dead cell staining assay

Gastric epithelial cells were seeded in 96-well plates at a density of 1×10^4 cells per well. After overnight cell attachment, the medium was replaced with 100 μL medium containing various concentrations (using the concentration of HKUST-1 as the reference) of CS@Lip@HKUST-1, Lip@HKUST-1, or HKUST-1, and the cells were incubated for 24 h, 48 h, and 72 h, respectively. Cell viability was assessed using the Cell Counting Kit-8 (CCK-8) assay. The culture medium was replaced with 100 μL of 10% CCK-8 dye solution per well. After incubating for 1 h at 37 °C, the water-soluble methotrexate dye was measured at a wavelength of 450 nm using a microplate reader (Molecular Devices SpectraMax[®] i3, USA). Three replicate wells were used for each group, and cell viability was calculated using the following Eq. (2):

$$\text{Cell viability (\%)} = \frac{(\text{OD}_{\text{experimental groups}} - \text{OD}_{\text{blank groups}})}{(\text{OD}_{\text{control groups}} - \text{OD}_{\text{blank groups}})} \times 100 \quad (2)$$

The live/dead cell staining assay was performed by replacing the medium with calcein-AM and PI dyes after the materials were cocultured with the cells. After incubating for 30 min at 37 °C, the cells were observed under a fluorescence inverted microscope (Leica, DMIL LED, Germany).

2.8. Hemolysis evaluation

Fresh blood was collected from rats and centrifuged at 5000 rpm (SCIOGEX, CF1524R, Beijing, China) for 5 min to remove the supernatant. Two milliliters of the collected blood was diluted to 50 mL with saline. Then, 300 μL of the diluted blood was mixed with 1.2 mL of saline containing different concentrations of CS@Lip@HKUST-1 (0, 20, 40, 60, 80, 100 $\mu\text{g}/\text{mL}$, using the concentration of HKUST-1 as the reference). As negative and positive controls, 300 μL of erythrocytes were added to 1.2 mL of saline and deionized water, respectively. The mixtures were incubated at 37 °C for 2 h, and the absorbance of the supernatant was measured at 540 nm using a microplate reader. The hemolysis rate was calculated using the following Eq. (3):

$$\text{Hemolysis rate (\%)} = \frac{(\text{OD}_{\text{experimental groups}} - \text{OD}_{\text{negative control group}})}{(\text{OD}_{\text{positive control group}} - \text{OD}_{\text{negative control group}})} \times 100 \quad (3)$$

2.9. Mucosa permeation studies

Using the Transwell system, we explored the transport capability of CS@Lip@HKUST-1 through the mucosa using previously reported method³⁵. In brief, freshly slaughtered pig mucosa was coated onto polycarbonate membranes with a pore size of 3 μm , and *H. pylori* suspension (1 mL) was present in the receptor chamber. Subsequently, fluorescently labeled CS@Lip@HKUST-1 (0.5 mL) was gently added to the mucosal surface, and the entire culture dish was incubated in a shaker at 37 °C (100 rpm). Every 6 h, 200 μL samples were taken from the receptor chamber, the value of OD_{600} was measured, and an equivalent amount of fresh PBS was replenished. Finally, fluorescence measurements were taken at the receptor site. The formula for calculating the apparent permeability coefficient (P_{app}) is as follows in Eq. (4):

$$P_{\text{app}} (\%) = (dQ/dt) \times 1 / (A \times C_0) \times 100 \quad (4)$$

where dQ/dt is the flux of fluorescently labeled CS@Lip@HKUST-1 from the donor side to the receptor side, C_0 is the initial concentration of CS@Lip@HKUST-1 in the donor chamber, and A is the membrane area (cm^2).

2.10. In vitro *H. pylori* antibacterial test

H. pylori was scraped from Columbia blood plates and resuspended in Brucella broth. The bacterial concentration was adjusted to 10^6 CFU/mL. Then, 10^6 CFU/mL bacteria were incubated with 10 mL of Brucella broth, 1 mL of FBS, 50 μL of mixed antibiotics, and 0.88 mg of the sample in a three-gas incubator with shaking for 24 h. After that, the mixture was diluted, and 20 μL of the diluted solution was spread evenly onto a blood agar plate. The plate was incubated for another 72 h, and the colonies on the plate were photographed and counted.

2.11. Scanning electron microscopy (SEM) morphological observation of *H. pylori*

H. pylori morphology was observed using SEM following methods described in the previous literature⁵³. Briefly, after coculture with the nanoparticles, the mixture was centrifuged at 5000 rpm (SCIOGEX, CF1524R) for 5 min, after which the supernatant was removed. The bacterial precipitate was collected and washed three times with PBS. Then, the supernatant was discarded, and a prechilled 2.5% glutaraldehyde solution was slowly added along the tube wall to fix the bacteria at 4 °C for more than 12 h. The solution was then dehydrated with different concentrations of ethanol and dispersed in *tert*-butanol. The mixture was freeze-dried on silicon wafers and sprayed with gold, after which the bacterial morphology was observed *via* SEM.

2.12. *H. pylori* live/dead staining test

After coculture with the sample, the *H. pylori* solution (1 mL) was added to SYTO 9/PI Live/Dead Bacterial Double Staining

Reagent (1.5 μ L SYTO 9 + 1.5 μ L PI) and incubated for 15 min in low light. The solution was then observed and photographed under an ortho-fluorescence microscope (MshOt, MF43-N, China). At least 10 visual fields from each group were randomly selected to count the number of live bacteria (green fluorescence).

2.13. *H. pylori* protein excretion test

After aspiration of the above suspension, the leaked protein concentration was measured using a Bradford protein assay kit according to the product instructions, and detected using a spectrophotometer at 595 nm. Cag A proteins (Santa Cruz Biotechnology, sc-28368, USA) were detected using Western blotting (WB) following methods described in the previous literature⁵⁴.

2.14. Urease activity of *H. pylori*

The urease activity of *H. pylori* after treatment with different groups was measured using urease activity kit and rapid urease test kit following the manufacturer's instructions. The tested samples are solutions obtained after coculturing bacterial suspensions with nanoparticles. In the rapid urease test, after co-incubating the sample with urease detection solution (0.9% NaCl, 20 mmol/L urea, 14 μ g/mL phenol red) in the test tube for 1 h, a photograph was taken, and then the OD value was measured at 550 nm using a spectrophotometer. While in the urease activity assay test, the urease activity of untreated bacterial suspensions serves as a reference to compare the mucosal activity after different treatments, expressed as a percentage.

2.15. Construction of the intracellular *H. pylori* model

The intracellular bacterial infection model was constructed as described in the references^{25,27}. Approximately 4×10^5 cells were inoculated in 6-well plates and incubated in a CO₂ incubator for 24 h. *H. pylori* was then added to the cell culture medium at a ratio of 100:1 MOI and incubated in a 37 °C incubator for 6 h to allow bacterial invasion into the cells. The cells were washed three times with PBS and incubated in medium containing 100 mg/L gentamicin for 1.5 h to kill extracellular bacteria. The number of intracellular bacteria was verified using three methods: CFU assay, PCR assay, and immunofluorescence staining.

CFU assay: The cells were incubated with 1% saponin at 37 °C for 15 min to increase cell membrane permeability. The cell suspension was then diluted and plated onto blood agar plates. After incubation for 5 days in a three-gas incubator, the colonies were counted.

PCR: *H. pylori* DNA was extracted using the Wizard Genomic Extraction Kit (Promega, A1120). The number of intracellular *H. pylori* was determined by determining the ratio of *H. pylori*-specific 16S DNA to Gapdh, as described in a previous reference²⁵. The primers used for detecting *H. pylori* DNA were as follows: forward primer: 5'-TTTT GTT AGA GAA GAT AAT GAC GGT ATC TAA C-3' and reverse primer: 5'-CAT AGG ATT TCA CAC CTG ACT GAC TAT C-3'. The primers for detecting human GAPDH DNA were as follows: forward primer: 5'-GAC TTC AAC AGC GAC ACC C-3' and reverse primer: 5'-AGA AGA TGA AAA GAG TTG TCA GGG C-3'. The relative expression of each gene was calculated using the $2^{-\Delta\Delta Ct}$ method as in Eq. (5):

Immunofluorescence staining: The cells were fixed with 4% paraformaldehyde at room temperature for 30 min. After washing with PBS, the cells were treated with 0.5% Triton-X100 for 15 min to increase cell membrane permeability. The cells were then washed with PBS and incubated overnight at 4 °C with 3% BSA and primary antibody (Abcam, 20459). The next day, the cells were washed with PBS and incubated with a secondary antibody (Abcam, 150080) at room temperature for 1 h. DAPI and an anti-fluorescence quencher (Thermo Fisher, P36981) were added after three washes with PBS, and the cells were observed using confocal laser scanning microscopy (CLSM, Olympus, FV1200).

2.16. Intracellular *H. pylori* antibacterial test

After constructing the intracellular *H. pylori* model as described above, the cells were treated with PBS, CS@RHL/CHOL@HKUST-1 (80 μ g/mL, with the concentration of HKUST-1 used as the reference), or CS@RHL/PA/CHOL@HKUST-1 (80 μ g/mL, with the concentration of HKUST-1 used as the reference) for an additional 24 h. The aforementioned methods (CFU assays, PCR assays, and immunofluorescence staining) were used to assess the intracellular survival of *H. pylori*.

2.17. Experiments on the mechanism of intracellular bacteria eradication

i) Autophagy-related experiments: immunofluorescence staining and Western blotting were used to measure the level of autophagy in cells after treatment with nanoparticles. After constructing the intracellular *H. pylori* model and treating it with nanoparticles, as described above, the protein was extracted from the cells and detected using a Bradford kit. Autophagy-related proteins were detected using WB following methods described in the previous literature²⁵. For immunofluorescence staining, the methods were as described above, and the primary antibodies used were SQSTM1/p62 (Servicebio, GB11531) and LC3-B (CST, 3868S). ii) Lysosomal acidification measurement: Lysosomal acidification was measured using the LysoSensor™ Green DND-189 probe. The intracellular *H. pylori* models treated with nanoparticles were incubated with the LysoSensor™ Green DND-189 probe at 37 °C for 1 h, and the green fluorescence intensity was observed using CLSM. iii) Cytosolic Ca²⁺ measurement: cytosolic Ca²⁺ levels were determined using Fura-2/AM (Yeasen, 40702ES50). The intracellular *H. pylori* models treated with nanoparticles were washed with PBS three times and incubated with Fura-2/AM (0.5 μ mol/L) for 30 min. After adding GPN (200 μ mol/L), the continuous fluorescence intensity of the cells was detected at excitation wavelengths of 340 and 380 nm over a certain period of time using a microplate reader.

2.18. Construction of the *H. pylori* biofilm model and eradication of *H. pylori* mature biofilms

H. pylori biofilms were cultured as described previously in the literature³¹. Briefly, *H. pylori* with an OD₆₀₀ value of 0.1 was cultured in confocal/24-well/96-well plates containing 5%

$$\Delta\Delta Ct = (Ct_{\text{experimental group target genes}} - Ct_{\text{experimental group internal reference genes}}) - (Ct_{\text{control group target genes}} - Ct_{\text{control group internal reference genes}}) \quad (5)$$

Brucella broth medium and incubated in a triple-air incubator without shaking for 3 days. The medium was then replaced with PBS, CS@RHL/PA/CHOL/@HKUST-1 (80 µg/mL, with the concentration of HKUST-1 used as the reference), or CS@PA/CHOL/@HKUST-1 (80 µg/mL, with the concentration of HKUST-1 used as the reference), after which the cells were incubated for another 24 h. The biofilm eradication effect was evaluated using crystal violet staining, CLSM, and SEM, as previously described³¹.

2.19. Penetration of nanoparticles in biofilms

The penetration of nanoparticles into the biofilm was studied using CLSM based on methods reported in previous studies²⁸. In brief, after successfully constructing the *H. pylori* biofilm, Cy-7-labeled nanoparticles were slowly added and cocultured for 1 and 2 h, respectively. After gentle washing three times with PBS, the biofilm was stained with DAPI for 20 min, and observation was performed using CLSM.

2.20. Cell scratch assay

The cells were evenly spread in a 6-well plate and starved. A scratch was made on the cell monolayer using a 10 µL pipette tip. The cells were then gently washed three times with PBS to remove floating cells. Subsequently, the cells were cocultured with or without AP@CS@Lip@HKUST-1 (80 µg/mL, using the concentration of HKUST-1 as the reference) at 37 °C. Images were captured at 0, 12, 24, 36, and 48 h. The cell migration rate was calculated using the following Eq. (6):

$$\text{Cell migration (\%)} = (\text{Scratch wound area at 0 h} - \text{Scratch wound area at testing time}) / \text{Scratch wound area at 0 h} \times 100 \quad (6)$$

2.21. In vivo *H. pylori* infection model

The *H. pylori* animal model was established following the methods described in previous literature²⁷. Six-week-old C57BL/6 mice were obtained from Jiangsu Collective Pharmachem Biotechnology Co (Nanjing, China). All mice were orally gavaged with 300 µL of *H. pylori* suspension (CFU/mL) once every other day for two weeks. After infection, the mice were kept under normal conditions for four weeks. Subsequently, five 10⁸ mice were randomly selected for execution, and their stomachs were taken for plate coating, urease tests, and H&E staining to evaluate the infection status. The Sydney system was used to evaluate the inflammation of the H&E images⁵⁵.

2.22. In vivo antimicrobial evaluation of *H. pylori* infection

H. pylori-infected mice were randomly divided into five groups ($n = 8$): PBS, Lip@HKUST-1 (8 mg/kg, with the concentration of HKUST-1 used as the reference), CS@Lip@HKUST-1 (8 mg/kg, with the concentration of HKUST-1 used as the reference), antibiotics (clarithromycin, 14.3 mg/kg/day), and AP@CS@Lip@HKUST-1 (8 mg/kg, with the concentration of HKUST-1 used as the reference). In detail, Lip@HKUST-1 and CS@Lip@-

HKUST-1 were administered to each mouse in the form of a solution by gavage. AP@CS@Lip@HKUST-1 was preloaded into a 1 mL syringe at a fixed volume and delivered into the stomach in a paste-like form through the syringe before it formed a hydrogel. Additionally, a control group without *H. pylori* infection and treated with PBS were included for comparison with the aforementioned five groups. On the second day after the completion of the treatment, all the mice were sacrificed, and the stomachs were imaged first. Then, they were cut longitudinally along the greater curvature. A portion of the stomach was ground in sterile distilled water, and a homogenate of the stomach tissue was taken to perform the plate coating test to assess *in vivo* antibacterial activity. Another portion of the stomach tissue homogenate was used to measure urease activity using a rapid urease test kit and urease activity kit following the methods described above. The remaining part of the stomach was subjected to H&E staining, and the content of *H. pylori* in the stomach tissue was assessed under a microscope.

2.23. Biological safety study

Following the above mentioned treatment, the heart, liver, spleen, lungs, and kidneys of mice were collected for H&E staining to evaluate animal safety. H&E staining was performed by Wuhan Servicebio Technology Co., Ltd. (Wuhan, China). Blood was collected from the mouse eyes for routine blood tests, and serum was obtained for liver and kidney function tests. Blood count, as well as liver and kidney function, were measured by Daixuan Biotechnology Co. (Shanghai, China).

2.24. In vivo anti-inflammatory evaluation

Enzyme-linked immunosorbent assay (ELISA) analysis and immunohistochemistry analysis were also conducted to evaluate the *in vivo* anti-inflammatory effects of the nanoparticles. Serum obtained from the treated mice was diluted and coincubated with ELISA detection solution (for MPO activity, IL-10, IL-6, IL-1β, IL-2, and IL-12) according to the instructions of the ELISA kit. The absorbance was measured at OD₄₅₀ nm. For immunohistochemistry analysis, after discontinuation of administration, stomach tissues were collected from the mice. The tissues were fixed, dehydrated with formaldehyde, and embedded in paraffin. Paraffin sections were prepared and subjected to immunohistochemical staining (TGF-β) to observe gastric inflammation. Immunohistochemistry analysis was performed by Wuhan Servicebio Technology Co., Ltd. (Wuhan, China).

2.25. In vivo mucosal repair evaluation

The stomachs of mice treated with AP@CS@Lip@HKUST-1, *H. pylori*-infected mice, and normal mice were collected to observe gastric tissue inflammation repair under optical light. Fluorescence staining was also performed to assess the status of gastritis repair *in vivo*. Ki67, β-catenin, and PCNA staining were performed to

evaluate the apoptosis of gastric epithelial cells, while ZO-1, Occludin-1, and Claudin staining were performed to evaluate the repair of the gastric mucosa. Fluorescence staining was performed by Wuhan Servicebio Technology Co., Ltd. (Wuhan, China).

2.26. Targeting adhesion experiments and in vivo metabolism of materials

AP@CS@Lip@HKUST-1 was labeled with Cy7 (MCE, HY-D0825) and administered to normal and *H. pylori*-infected mice ($n = 5$) via gavage with Cy7-labeled AP@CS@Lip@HKUST-1. After 8 h, the gastric and ileal tissues were imaged using the IVIS imaging system (Tanon ABL X6, China).

2.27. Penetration of nanoparticles in biofilms

After a one-day fasting period, *H. pylori*-infected mice ($n = 6$) were gavaged with Cy7-labeled CS@Lip@HKUST-1. Subsequently, the mice were euthanized at 0, 15, 30 min, 1, 1.5, and 2 h after gavage, and the gastric tissue was imaged using an IVIS imaging system.

2.28. Gut microbiota analysis

Fecal samples were collected from each group of mice on the second day after the completion of treatment. The abundance and diversity of bacteria in the mouse feces were determined using 16S rRNA sequencing. The analysis was conducted by Daixuan Biotechnology Co. (Shanghai, China).

2.29. Transcriptomic analysis

Gastric tissues from mice treated with PBS and AP@CS@Lip@HKUST-1, as well as normal mice, were obtained for transcriptional analysis to identify genetic differences in mice treated with AP@CS@Lip@HKUST-1. The experiments were conducted by Major Biomedical Technology Co. (Shanghai, China).

2.30. Total RNA extraction

Total RNA was extracted from tissues using TRIzolTM according to the instructions. Briefly, 60 mg of tissues were weighed and ground into powder in liquid nitrogen while homogenizing for 5 min. After resting for 5 min, the tissues were centrifuged at $12,000 \times g$ for 5 min at 4 °C; the supernatant was then transferred to a new tube containing 0.3 mL of chloroform/isoamyl alcohol (24:1). Then, the samples were centrifuged again for 10 min (4 °C, 12,000 rpm, ROTINA, 420R, Kirchlengern, Germany), and the supernatant with retained RNA was transferred to a new tube with an equal amount of isopropanol solution and centrifuged again for 20 min (4 °C, 13,600 rpm, ROTINA, 420R). After removing the supernatant, it was washed twice with 1 mL of 75% ethanol; the remaining ethanol was collected by centrifugation for 2 min (4 °C, 13,600 rpm, ROTINA, 420R) and then air-dried in a biosafety cabinet for 5 min. Finally, diethyl pyrocarbonate-treated water was added to dissolve the RNA for 25–100 μ L. Subsequently, the RNA was analyzed using an Agilent 2100 Bioanalyzer (Thermo Fisher Scientific, MA, USA) for the identification and quantification of total RNA.

2.31. Statistical analysis

All data are expressed as the mean \pm standard deviation (SD). Statistical analyses were performed using R statistical software 3.6.1 (www.r-project.org). The difference between the two groups was compared using Student's *t*-test, while the difference between three or more groups was compared using one-way ANOVA. *P* value < 0.05 was considered statistically significant (ns: not significant, **P* < 0.05, ***P* < 0.01, and ****P* < 0.001).

3. Results and discussion

3.1. Synthesis and characterization of CS@Lip@HKUST-1

The strategy for synthesizing HKUST-1 nanoparticles for the delivery and slow release of Cu²⁺ is shown in Fig. 1. X-ray photon spectroscopy (XPS) showed that the HKUST-1 nanoparticles comprised Cu, C and O, with Cu²⁺ as the core metal and trimesic acid (H₃BTC) as the ligand skeleton, which was consistent with the reported composition of HKUST-1 (Fig. 1A)⁵⁶. The Cu 2p and Cu LM2 spectra showed electron binding energies of 954.28, 934.38, and 571.08 eV, corresponding to Cu 2p^{1/2}, Cu 2p^{3/2}, and Cu LM2, respectively (Supporting Information Fig. S1A and S1B). Additionally, an electron binding energy of 284.38 eV in the C 1s and O 1s spectra corresponded to aromatic carbon (C–C), 288.18 eV corresponded to carboxylic acid carbon (–COOH), and 531.28 eV corresponded to carboxylic acid oxygen (O–C=O) (Fig. S1C and S1D). Integration of the characteristic peak areas indicated that Cu, C and O accounted for 8.02%, 59.14% and 32.84%, respectively. To further validate the successful preparation of HKUST-1, the crystal phases were characterized by X-ray crystallography (XRD), which revealed a cubic crystal structure with an average crystal length of 26.20 Å, which was consistent with previous reports^{57,58}. The diffraction peaks at 11.663°, 13.425°, 17.558°, and 19.118° represented distances of 222, 400, 500, and 440° between lattice planes, respectively (Fig. 1B).

Morphological examination by scanning electron microscopy (SEM) and transmission electron microscopy (TEM) confirmed that HKUST-1 nanoparticles were porous and spherical on the surface (Fig. 1C and D(a)), while a bright band observed by TEM of Lip@HKUST-1 and CS@Lip@HKUST-1 indicated that HKUST-1 was successfully enveloped in RHL/PA/CHOL liposomes and CS (Fig. 1D (b and c)), and the LCMS result showed that RHL accounted for 46.33% of the overall liposome mass (Supporting Information Fig. S2). Additional TEM elemental mapping showed that C, O and Cu were uniformly distributed in the nanoparticles (Supporting Information Fig. S3). Examination of the average particle size of HKUST-1, Lip@HKUST-1, and CS@Lip@HKUST-1 indicated that they averaged 204.66 nm, 233.03 nm, and 273.77 nm in diameter, respectively (Supporting Information Fig. S4), corresponding to incremental size increases with the addition of successive lipid and chitosan layers from HKUST-1 to Lip@HKUST-1 and CS@Lip@HKUST-1. In addition, we examined the particle size and potential changes of Lip@HKUST-1 and CS@Lip@HKUST-1 over 7 days, and the results showed that Lip@HKUST-1 and CS@Lip@HKUST-1 have high stability (Supporting Information Fig. S5). In our study, we used liposomes as our anti-*H. pylori* formulation for the following three reasons: first, both PA and rhamnolipids are lipids, and they could be well mixed with other lipids to formulate

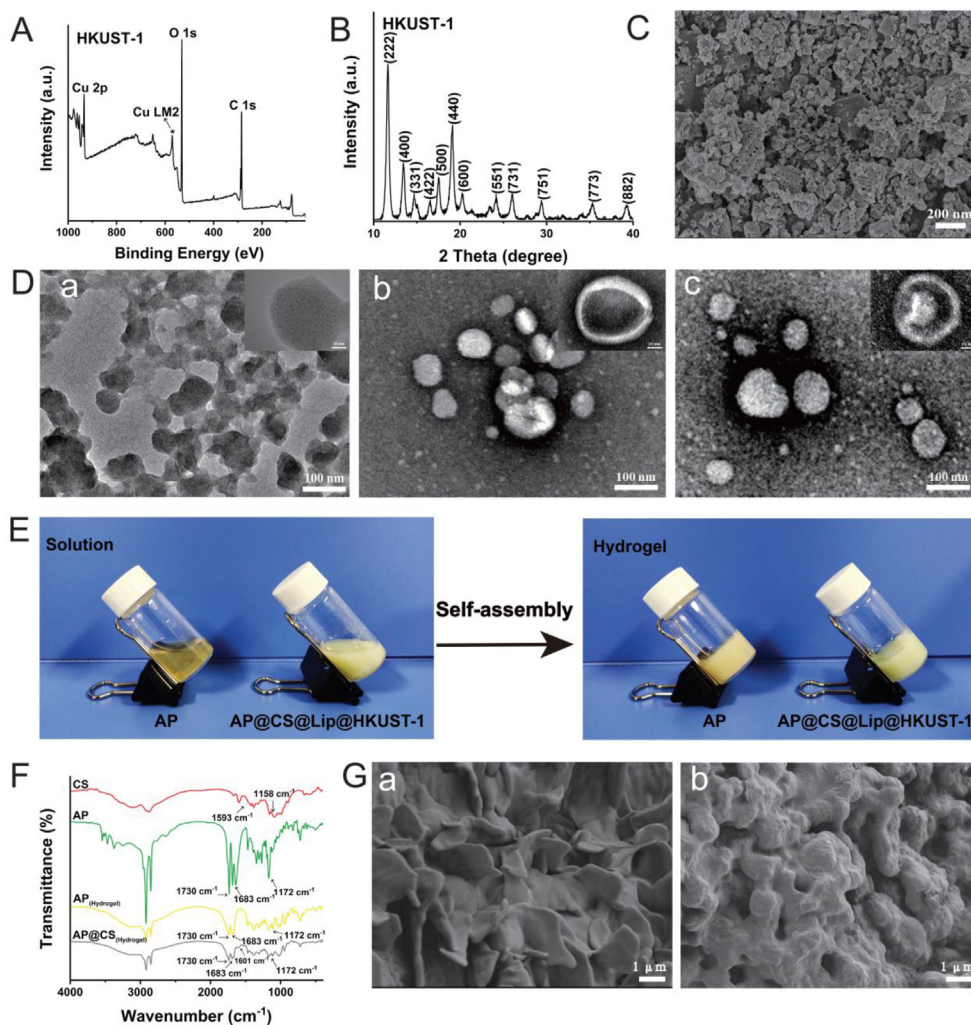


Figure 1 Characterization of nanoparticles and hydrogels. (A) XPS spectra of Cu 2p, Cu LM2, O 1s, and C 1s in HKUST-1. (B) XRD patterns of HKUST-1. (C) SEM image of HKUST-1 in PBS, bars represent 200 nm. (D) TEM images of HKUST-1 (a), Lip@HKUST-1 (b), and CS@Lip@HKUST-1 (c), bars represent 100 nm; enlarged Figure: bars represent 10 nm. (E) Optical images of AP hydrogels and AP@CS@Lip@HKUST-1 before and after hydrogel formation. (F) FTIR transmission spectra of CS, AP, AP hydrogels, and AP@CS@Lip@HKUST-1. (G) SEM images of the AP hydrogel (a) and AP@CS@Lip@HKUST-1 (b), bars represent 1 μ m.

liposomes; second, liposomes have good biocompatibility and represent the most common nanomedicines at present; and finally, negatively charged liposomes could be well coated by positively charged chitosan due to electrostatic interactions. Taken together, these results confirmed the successful generation of CS@Lip@HKUST-1 nanoparticles.

Since Cu^{2+} was adopted as the primary antimicrobial component to eradicate *H. pylori* and subsequently promote mucosal repair, we compared the rates of Cu^{2+} release from HKUST-1 and CS@Lip@HKUST-1 in simulated gastric fluid (SGF). Inductively coupled plasma–mass spectrometry (ICP–MS) analysis indicated that 94.6% of Cu^{2+} was released from HKUST-1 into SGF within 4 h of incubation, whereas only 48.9% of Cu^{2+} was released from CS@Lip@HKUST-1 in the same time period, and 94.2% was released by 12 h (Supporting Information Fig. S6). These results suggested that the addition of liposomes and chitosan layers could indeed significantly decrease the rate of Cu^{2+} release, potentially prolonging the antibacterial and tissue regeneration-promoting effects of the nanoparticles.

3.2. Characterization and inflammation targeting ability of AP@CS@Lip@HKUST-1

The high acidity conditions in the stomach coupled with the ability of *H. pylori* to below the gastric mucosa both contribute to steadily increasing drug resistance and the limited effectiveness of many conventional drugs toward this pathogen²³. These factors suggest that targeting *H. pylori* aggregation sites may be an effective strategy for suppressing *H. pylori* populations. Furthermore, *H. pylori* infection commonly results in localized sites of inflammation in the gastric mucosa, which exhibit a characteristic positive charge accompanied by increased MMP secretion⁵⁹. Thus, AP, which can self-assemble into a stable, negatively charged hydrogel under acidic conditions, can be rapidly degraded by MMP, suggesting that it might be an effective material for alleviating local inflammation in the gastric mucosa.

Here, CS@Lip@HKUST-1 was encased in AP and formed a hydrogel (Fig. 1E). Analysis with a ZetaSizer Nano-ZS 90 showed that CS@Lip@HKUST-1 carried a positive zeta potential, while

AP@CS@Lip@HKUST-1 had a negative zeta potential, which could facilitate the targeting of inflammatory sites in the stomach (Supporting Information Fig. S7). We thus hypothesized that MMP degradation of the AP layer could enhance the release of CS@Lip@HKUST-1, promoting its bactericidal activity toward *H. pylori* via charge-based interactions. To further validate the molecular structure of this AP self-assembled hydrogel, we used Fourier transform-infrared spectroscopy (FT-IR) to analyze the functional groups and chemical bonds of the AP hydrogel molecular spectrum. The results identified 1172 cm^{-1} peak corresponding to the ester bond (C–O–C) of ascorbic acid, an absorption peak at 1683 cm^{-1} corresponding to the carbon-carbon double bond (C=C) in the ascorbic acid group, and three absorption peaks at 3546 , 3469 and 3372 cm^{-1} corresponding to the three hydroxyl groups (–OH) in the palmitic acid molecule, which are hydrophilic groups in the ascorbic acid molecule. In addition, we also found hydrophobic groups in palmitic acid molecules, such as the large 2918 cm^{-1} peak with high methylene (–CH₂–) content and the carbonyl group (C=O) at 1730 cm^{-1} (Fig. 1F)^{59,60}. However, in the molecular spectra of the AP hydrogels, the number of hydroxyl and methylene groups was less than that of the AP molecules. These results thus indicated that the self-assembled AP hydrogels were successfully constructed through hydrophobic and hydrophilic interactions.

Similar analysis of the CS molecule spectrum showed an absorption peak at 1158 cm^{-1} corresponding to an ether bond (C–O–C) and a characteristic peak at 1593 cm^{-1} for the primary amino group (–NH₂) of chitosan. These results indicated that chitosan was positively charged and could be used to construct hydrogels with negatively charged AP through electrostatic interactions, which was supported by analysis of AP@CS hydrogel spectra that showed an overall reduced content of chitosan primary amino groups (Fig. 1F). Further SEM observation of the AP hydrogel and AP@CS@Lip@HKUST-1 surface morphology (Fig. 1G) revealed the presence of scale-like structures on the AP hydrogel (Fig. 1G(a)), aligning well with the findings of a previous study⁶⁰. In addition, many round bumps were found on the hydrogel surface after loading CS@Lip@HKUST-1, presumably formed by the encapsulation of nanoparticles in the hydrogel (Fig. 1G(b)).

Then, the rate of enzymatic degradation of the AP hydrogel was investigated, which showed that only ~25% of the AP hydrogel degraded within 20 h in PBS (Supporting Information Fig. S8A). In contrast, the degradation rate markedly increased in the presence of collagenase IV, with >90% of the AP hydrogel degrading within 6 h. Supporting Information Figs. S8B and S9 further validate the stability of AP in acidic environments and PBS, which demonstrates that the hydrogel remains stable in both acidic and neutral environments. Additionally, we explored the minimum collagenase IV concentration for the degradation of the AP hydrogel (Fig. S8C). The results indicate that, the AP hydrogels exhibited a degradation pattern comparable to that observed in PBS when exposed to a collagenase IV concentration of 0.015625 mg/mL . We next sought to verify that AP@CS@Lip@HKUST-1 indeed targeted inflammatory sites in mice that were infected or not infected with *H. pylori*. To this end, infected mice and uninfected mice were orally administered Cy7-labeled AP@CS@Lip@HKUST-1 and then sacrificed after 8 h. IVIS imaging of the gastric tissues showed a strong fluorescent signal in mice with *H. pylori* infection with a large amount of fluorescent residue in the stomach samples, whereas uninfected control mice had obviously lower fluorescence in stomach tissue

($P < 0.001$) (Supporting Information Fig. S10). Examination of intestinal samples showed markedly lower fluorescence, validating that AP@CS@Lip@HKUST-1 preferentially targeted sites in the stomach (Supporting Information Fig. S11).

3.3. Cytotoxicity and anti-*H. pylori* activity of CS@Lip@HKUST-1 *in vitro*

In the proposed bactericidal mechanism for eliminating *H. pylori* by AP@CS@Lip@HKUST-1 (Fig. 2A), the AP hydrogel targets local inflammation sites in the stomach corresponding to *H. pylori* aggregation and is then hydrolyzed by secreted MMPs, releasing CS@Lip@HKUST-1 to target *H. pylori* through electrostatic attraction between CS and *H. pylori*^{42,43,61}. In the presence of gastric acids, Cu²⁺ is slowly released from nanoparticles, compromising *H. pylori* cell membrane integrity and resulting in membrane rupture and cell death. Additionally, CS@Lip@HKUST-1 can inhibit the urease activity of *H. pylori* and effectively kill *H. pylori* by promoting sensitivity to gastric acid.

For clinical gastric applications, favorable biocompatibility should be the primary consideration. To investigate the safety and biocompatibility of the HKUST-1, Lip@HKUST-1, CS@Lip@HKUST-1, and AP@CS@Lip@HKUST-1 biomaterials, we treated HFE-145 gastric epithelial cells with each nanoparticle type (at different concentrations) and examined cell viability after 1, 2, and 3 days through a CCK-8 assay. The results confirmed that each of the four treatment groups was higher than 80% when the concentration of nanoparticles was $80\text{ }\mu\text{g/mL}$ (using the concentration of HKUST-1 as the reference) (Supporting Information Fig. S12A–S12D). Additionally, live/dead cell staining assays showed a high live cell rate (green fluorescence) of CS@Lip@HKUST-1 after 1, 2, and 3 days of coculture with gastric epithelial cells (Fig. 2B, Supporting Information Figs. S13 and S14). Next, a hemolysis assay was performed to evaluate the blood compatibility of CS@Lip@HKUST-1, with PBS as the negative control and water as the positive control. Similarly, erythrocyte hemolysis assays showed that CS@Lip@HKUST-1 ($80\text{ }\mu\text{g/mL}$) had excellent blood compatibility, with a hemolysis rate of 0.6%, and the mouse red blood cells readily separated from the solution (Supporting Information Fig. S15).

After the hydrolysis of AP, the released CS@Lip@HKUST-1 becomes the primary effective substance for eradicating *H. pylori* in the stomach. Therefore, the retention time of CS@Lip@HKUST-1 in the stomach is the first issue we need to explore. As shown in Supporting Information Fig. S16, the fluorescence of Cy7-labeled CS@Lip@HKUST-1 remained present in the mouse stomach within 2 h after administration, indicating that CS@Lip@HKUST-1 can persist in the mouse stomach for at least 2 h. We speculate that CS imparts the ability for nanoparticles to penetrate the mucosal barrier, thereby increasing the retention time of nanoparticles in the stomach^{9,62}. To further investigate this phenomenon, we explored the ability of CS@Lip@HKUST-1 to penetrate the gastric mucus barrier *in vitro* (Supporting Information Fig. S17A). As shown in Fig. S17B, the P_{app} values of HKUST-1, Lip@HKUST-1, and CS@Lip@HKUST-1 were 1.06×10^{-5} , 4.15×10^{-5} , and $1.08 \times 10^{-4}\text{ cm/s}$, respectively. These findings indicate that, compared to HKUST-1 and Lip@HKUST-1, CS@Lip@HKUST-1 has superior mucosal penetration effects. Furthermore, by determining the viability of *H. pylori* beneath the mucosa, we further confirmed the mucosal penetration of CS@Lip@HKUST-1, suggesting that CS@Lip@HKUST-1 has stronger antibacterial activity than

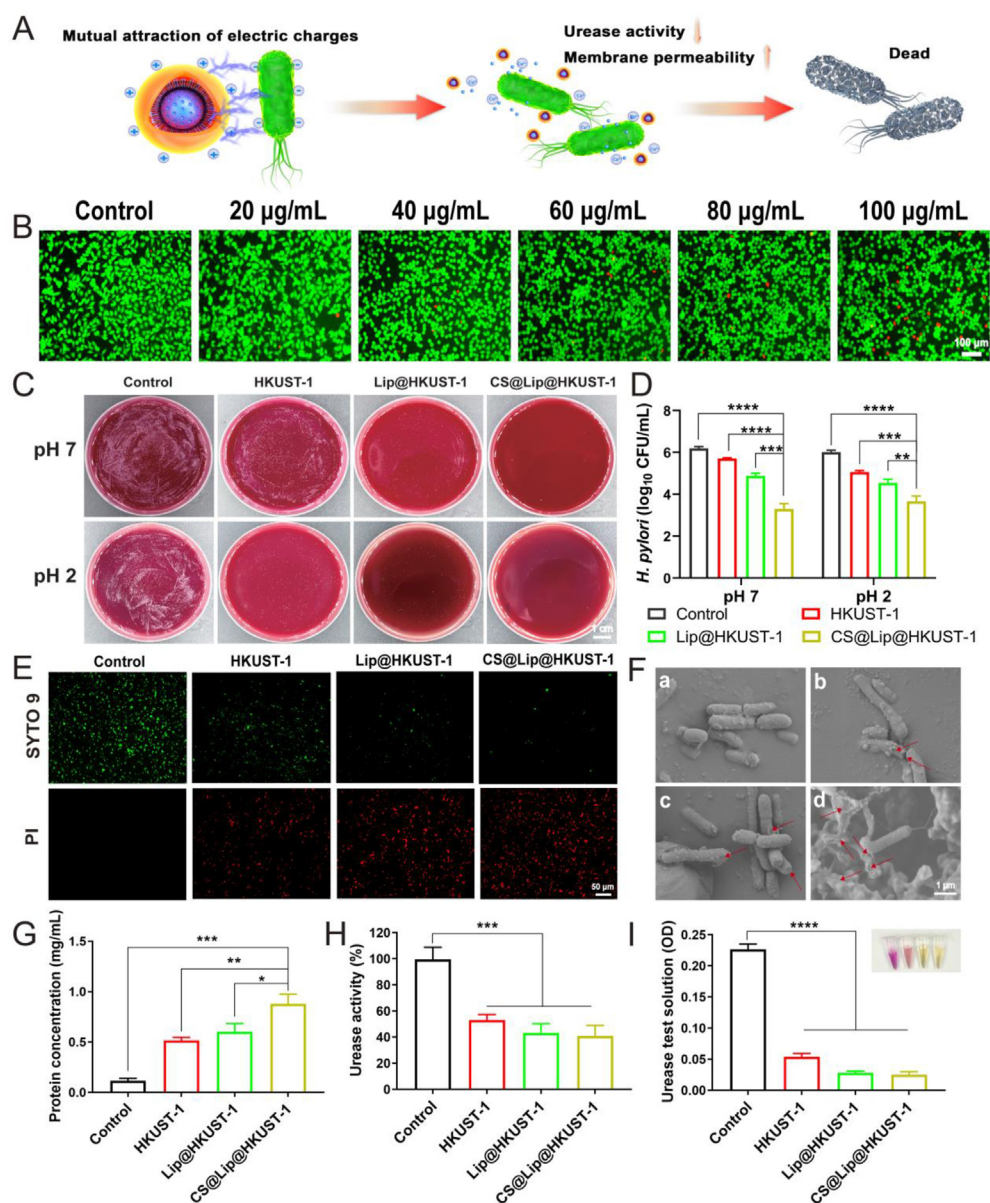


Figure 2 Antibacterial abilities of nanoparticles *in vitro*. (A) The antibacterial mechanism of CS@Lip@HKUST-1. CS@Lip@HKUST-1 targets *H. pylori* by electrostatic attraction and subsequently destroys the *H. pylori* bacterial membrane by slowly releasing Cu^{2+} while inhibiting *H. pylori* urease activity. (B) Live/dead cell staining of HFE-145 cells after coculture with CS@Lip@HKUST-1 for 3 days; bars represent 100 µm. Colony plate images (C) and colony count plots (D) of different samples after coculture with *H. pylori* under acidic (pH = 2) and neutral (pH = 7) conditions; bars represent 1 cm. (E) Live (green fluorescence)/dead (red fluorescence) bacterial staining of *H. pylori* after coculture with different treatments; bars represent 50 µm. (F) Morphological changes in *H. pylori* in SEM images after treatments, red arrows represent bacterial membrane breaks; bars represent 1 µm. (G) Bradford kit to detect *H. pylori* overflow protein concentration after different treatments. (H) The urease activity of *H. pylori* after treatments was measured by a urease activity kit. (I) Absorption spectra of urease detection solution (532 nm) of *H. pylori* after treatment. Data are presented as the mean ± SD ($n = 3$), * $P < 0.05$, ** $P < 0.01$, *** $P < 0.001$, **** $P < 0.0001$. ns, not significant.

HKUST-1 and Lip@HKUST-1 (Fig. S17C). In conclusion, we conclude that CS@Lip@HKUST-1 has excellent mucosal penetration ability, allowing nanoparticles to persist in the stomach for at least 2 h.

To experimentally characterize the bactericidal effects, we examined colony formation on agar plates containing HKUST-1, Lip@HKUST-1, and CS@Lip@HKUST-1 and found that the CS@Lip@HKUST-1 treatment showed the strongest antibacterial

effects, followed by Lip@HKUST-1, in both neutral and acidic environments (Fig. 2C and D). It is likely that the enhanced antibacterial properties of Lip@HKUST-1 over HKUST-1 might be attributable to increased nanoparticle uptake by *H. pylori*⁹, which was further increased by the intrinsic antimicrobial properties of CS and the electrostatic interaction between CS and *H. pylori*^{42,62}. Subsequent live/dead staining assays showed that the CS@Lip@HKUST-1 possesses excellent antibacterial activity, as

indicated by the large amount of red fluorescence observed after treatment with CS@Lip@HKUST-1 (Fig. 2E, Supporting Information Fig. S18). SEM imaging also depicted obvious membrane damage and cell death (red arrow) increasing in severity from HKUST-1 to Lip@HKUST-1, most prominently in cells treated with CS@Lip@HKUST-1 (Fig. 2F).

In light of these data, we then investigated the antibacterial mechanism of action for these nanoparticles. Quantification of total protein extracts in culture supernatants showed that all the treatments could significantly induce the loss of protein compared with the untreated control. Notably, the greatest loss of protein occurred in the CS@Lip@HKUST-1 group, followed by the Lip@HKUST-1 and HKUST-1 groups (Fig. 2G). Then, *H. pylori*-specific protein (Cag A) levels in the supernatant were analyzed using the WB assay, and the results were consistent with the above protein quantification assay (Supporting Information Fig. S19). We also found that CS@Lip@HKUST-1 conferred the strongest significant inhibition of *H. pylori* urease activity compared with that in controls (Fig. 2G and H). In summary, CS@Lip@HKUST-1 appeared to disrupt the *H. pylori* cell membrane and induce protein leakage while also inhibiting urease activity and leading to bacterial death. Notably, compared with previous studies, CS@Lip@HKUST-1 adopts a novel antibiotic-free antimicrobial strategy with both targeting and inhibition of urease activity, thereby destroying the survival environment of *H. pylori*, which makes it very difficult for *H. pylori* to develop drug resistance^{30,35,63}.

3.4. Antibiofilm activity of CS@Lip@HKUST-1 toward *H. pylori*

Biofilm, formed by *H. pylori* strains, is a protective barrier that can avoid exposure to antibiotics while also reportedly exhibiting higher rates of horizontal gene transfer and upregulation of drug resistance efflux pumps, consequently promoting the likelihood of developing drug resistance and increasing survival rates under antibiotic exposure²³. Thus, it is imperative to endow nanoparticles with an eradication effect on *H. pylori* biofilms. To improve nanoparticle efficacy toward biofilm-forming strains, we applied RHL to the outer lipid layer based on its reported effects in binding metal ions inside EPS and interrupting the signaling pathway (Fig. 3A)^{28,35}. Thus, we hypothesized that increasing *H. pylori* exposure to CS@Lip@HKUST-1 could increase cytotoxicity while precluding or inhibiting biofilm reformation³⁵. TEM imaging and crystal violet staining of *H. pylori* biofilm confirmed that *H. pylori* was tightly aggregated within an extracellular matrix, indicating that the *H. pylori* biofilm model was successfully constructed (Supporting Information Figs. S20 and S21). The application of prepared nanoparticles can significantly enhance their antibiofilm efficacy if they can efficiently penetrate biofilms. Therefore, our scrutiny focused on the penetration of nanoparticles into the *H. pylori* biofilm using CLSM. Our findings revealed that CS@Lip@HKUST-1 exhibited a superior penetration rate within the *H. pylori* biofilm, rapidly infiltrating the biofilm within 1 h (Supporting Information Fig. S22). In contrast, Lip@HKUST-1, even after 2 h, exhibited limited penetration into the *H. pylori* biofilm. This disparity may be ascribed to the positively charged surface of CS@Lip@HKUST-1, which interacts with the abundant negatively charged components in the biofilm.

Next, we examined whether adding RHL to the liposomal layer of CS@Lip@HKUST-1 inhibited *H. pylori* biofilm formation via

quantitative analysis of crystal violet staining. As shown in Supporting Information Fig. S23, compared with CS@Lip@HKUST-1 (No RHL), treatment with CS@Lip@HKUST-1, which contained RHL, indeed inhibited biofilm formation, and CS@Lip@HKUST-1 presented a biofilm eradication effect in a dose-dependent manner, which could eliminate more than 90% of the biofilm compared to controls at a concentration of 80 $\mu\text{g/mL}$ (Supporting Information Fig. S24).

In addition, we also used CLSM for live-dead staining of biofilms, which showed that both cell density and viability dramatically (green fluorescence) decreased in *H. pylori* biofilms treated with CS@Lip@HKUST-1 but not CS@Lip@HKUST-1 (No RHL) (Fig. 3B). Furthermore, SEM was performed for morphological examination after different treatments, and the results indicated that treatment with CS@Lip@HKUST-1 (No RHL) resulted in disruption, but not clearance, of the biofilm. In contrast, exposure to CS@Lip@HKUST-1 resulted in complete clearance of the *H. pylori* biofilm (Fig. 3C).

Taken together, these results demonstrated that CS@Lip@HKUST-1 can rapidly permeate biofilms and that the addition of RHL to the liposome layer could markedly enhance the antibacterial effects of CS@Lip@HKUST-1 in clearing *H. pylori* in biofilms.

3.5. PA-dependent clearance of intracellular *H. pylori* via autophagy rescue *in vitro*

In addition to biofilm formation, *H. pylori* may also reside within host cells, sporadically emerging, disseminating, and recolonizing gastric mucosa, consequently resulting in treatment failure and recurring infection⁹. In addition, Xie et al.²⁷ indicated that these intracellular *H. pylori* may inhibit autophagy, inducing a DNA damage response and ultimately leading to tumorigenic transformation in gastric cells. Eliminating intracellular *H. pylori* is therefore critical to reducing the risk of persistent infections as well as the incidence of gastric cancer. In the current study, we established an *in vitro* model of intracellular *H. pylori* using a previously published method²⁷ in which *H. pylori* was stained red for CLSM imaging around the nucleus of HFE-145 gastric epithelial cells (Supporting Information Fig. S25), verifying that the bacteria had indeed entered the cell. Intracellular *H. pylori* cells were also detected through qPCR analysis, in which *H. pylori*-infected cells expressed higher levels of *H. pylori* 16S rDNA than the control group ($P < 0.001$) (Supporting Information Fig. S26). These validation results indicated that the intracellular bacterial infection model was successfully established.

Then, we examined whether HKUST-1-derived nanoparticles could decrease the viability of intracellular *H. pylori*. Plate counts of *H. pylori* in HFE-145 lysates showed that intracellular *H. pylori* exposed to CS@Lip@HKUST-1 formed significantly fewer colonies ($P < 0.05$) than other treatment groups (Fig. 4A, Supporting Information Fig. S27), whereas CS@Lip@HKUST-1 (No PA) had no obvious effect on bacteria. Moreover, qPCR analysis showed that intracellular *H. pylori* DNA levels were significantly lower in cells treated with CS@Lip@HKUST-1 than in the untreated control or CS@Lip@HKUST-1 groups (No PA) ($P < 0.05$) (Fig. 4B). Additionally, CLSM imaging indicated that intracellular colonization by *H. pylori* (red fluorescence) was significantly decreased after treatment with CS@Lip@HKUST-1 (Fig. 4C, Supporting Information Fig. S28).

Based on the above results, we then explored the possible mechanisms through which CS@Lip@HKUST-1 could suppress

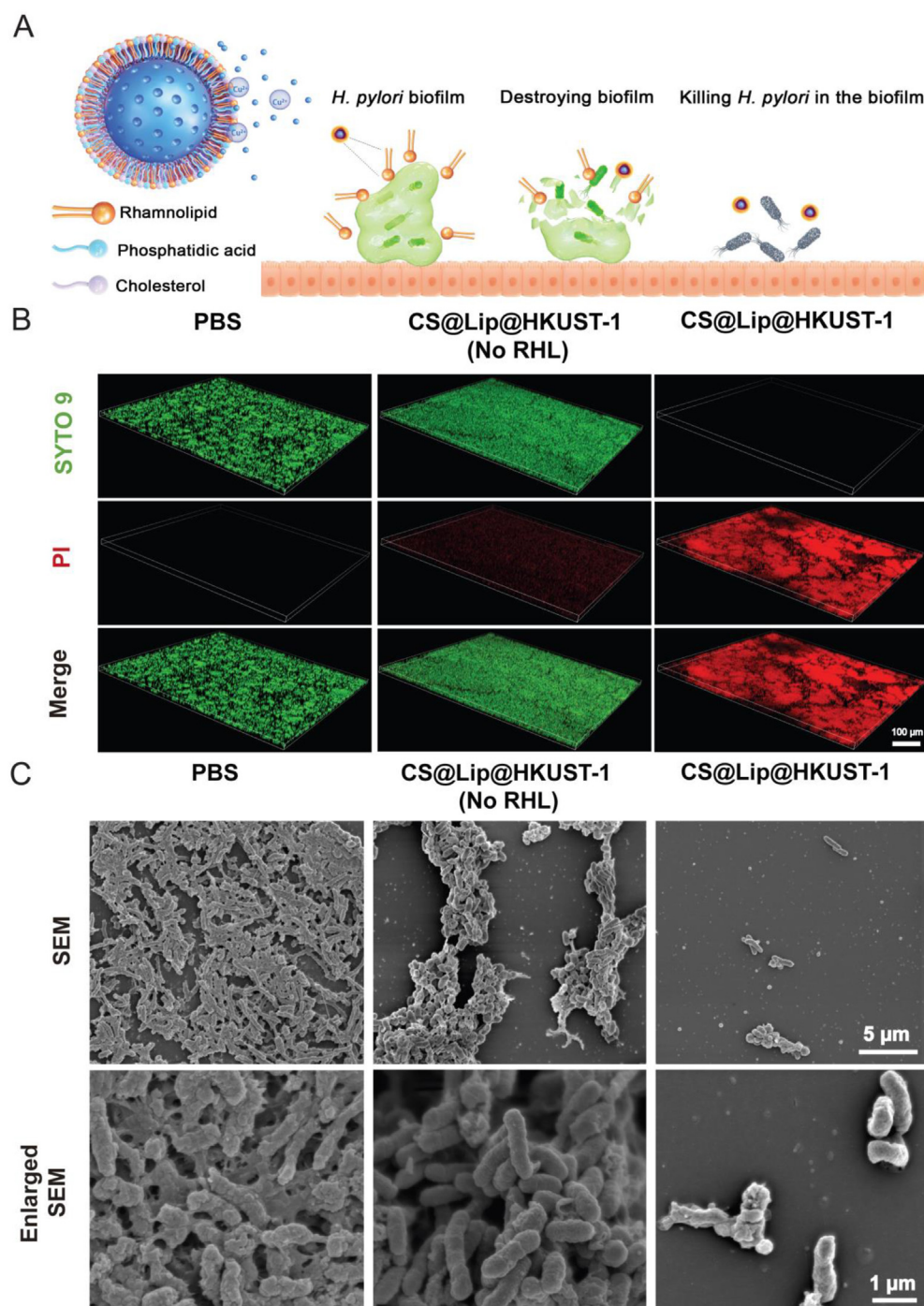


Figure 3 Antibiofilm activity of nanoparticles against *H. pylori*. (A) The antibiofilm mechanism of CS@Lip@HKUST-1. Nanoparticles penetrate into the biofilm and destroy the biofilm through RHL, which then kills *H. pylori* in the biofilm. (B) CLSM images of *H. pylori* biofilms after different treatments. The biofilm was stained with SYTO 9 (green: live bacteria) and PI (red: dead bacteria), scale: 100 μm . (C) SEM images of *H. pylori* biofilms architecture after different treatments, SEM scale: 5 μm ; Enlarged SEM scale: 1 μm .

intracellular *H. pylori*. *H. pylori* survival in host cells was previously shown to depend on the inhibition of Ca^{2+} efflux from lysosomes, which in turn inhibits lysosomal acidification and cellular autophagy^{25,27,28}. Conversely, PA was previously shown to promote Ca^{2+} efflux, inducing lysosomal acidification and subsequently resulting in host cell elimination of intracellular *Mycobacterium tuberculosis*³⁸. In this context, we hypothesized that the PA in CS@Lip@HKUST-1 might also promote host

elimination of intracellular *H. pylori* via lysosomal acidification and induction of host autophagy. To test this possibility, we explored whether and how PA affected autophagy by quantifying the autophagy marker proteins p62 and LC3 in HFE-145 cells treated with CS@Lip@HKUST-1. Western blot analysis showed that p62 protein levels increased while LC3 B III/I decreased in untreated cells infected with *H. pylori* compared to uninfected untreated control cells (Fig. 4D and E), suggesting that *H. pylori*

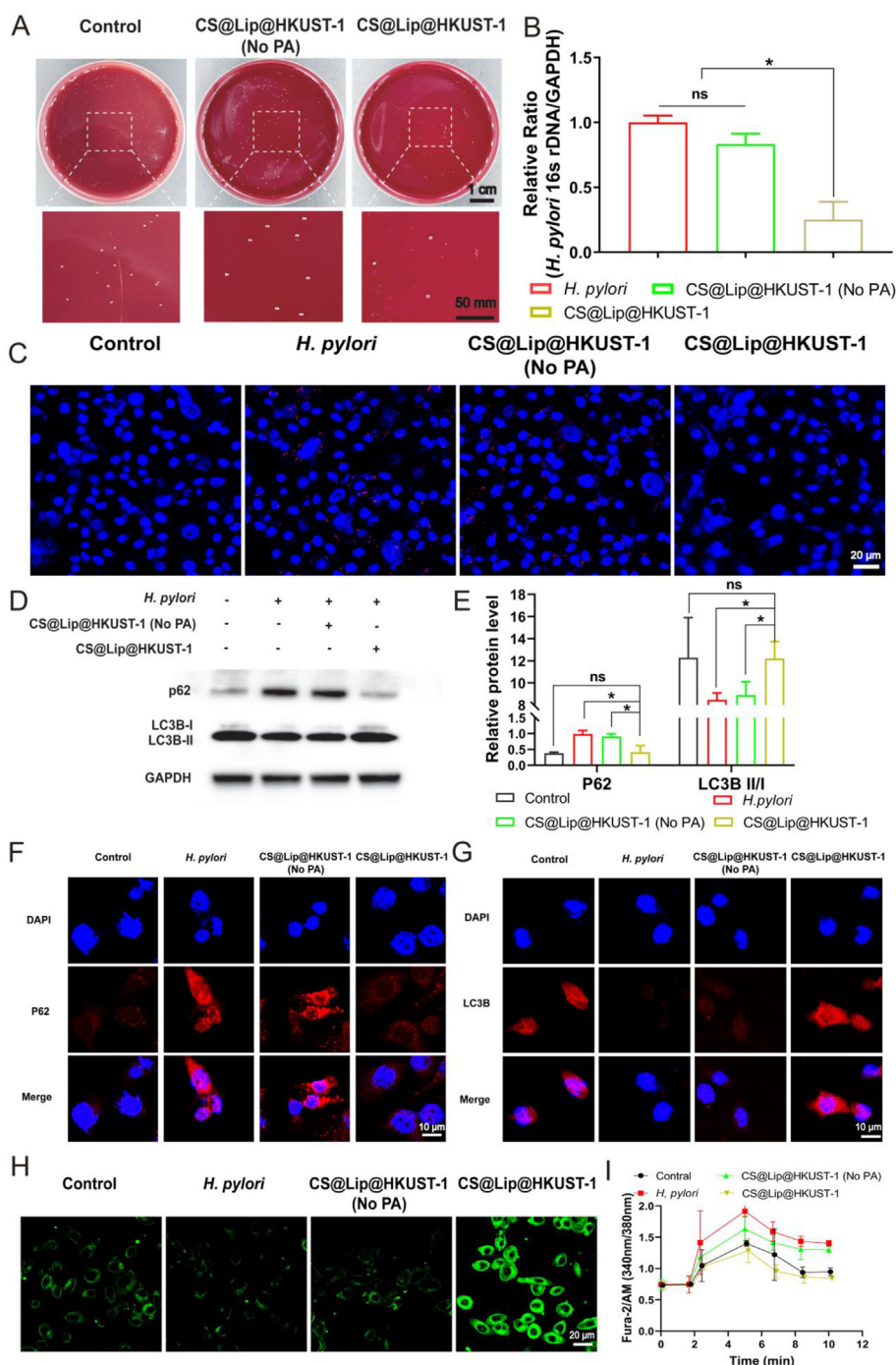


Figure 4 Killing ability of CS@Lip@HKUST-1 against intracellular *H. pylori*. (A) After coculturing the *H. pylori* model with nanoparticles, the intracellular *H. pylori* concentration was visualized using a plate assay. (B) Relative expression of intracellular *H. pylori* DNA after different treatments. (C) CLSM images of intracellular *H. pylori* content after different treatments, cell nucleus (in blue), and *H. pylori* (in red rods); scale: 20 μm . (D) After coculturing the intracellular *H. pylori* model with nanoparticles, whole-cell lysates were collected to examine LC3B and P62 protein levels by Western blotting, and (E) the LC3B-II:LC3B-I ratio and relative P62 protein levels were quantified. CLSM images are shown for (F) P62 and (G) LC3B protein expression in HFE-145 cells after coculturing the intracellular *H. pylori* model with nanoparticles, scale: 10 μm . (H) Lysosomal acidification levels in HFE-145 cells after coculturing the intracellular *H. pylori* model with nanoparticles; scale: 20 μm . (I) Lysosomal calcium levels in HFE-145 cells after coculturing the intracellular *H. pylori* model with nanoparticles. Data are presented as the mean \pm SD ($n = 3$), * $P < 0.05$, ** $P < 0.01$, *** $P < 0.001$, **** $P < 0.0001$. ns, not significant.

might inhibit early autophagy in host cells to evade elimination by the host, which is consistent with previous studies^{25,27}. In *H. pylori*-infected HFE-145 cells treated with CS@Lip@HKUST-1 (No PA), no obvious change was found in either p62 or LC3B II/I

expression, while the addition of CS@Lip@HKUST-1 resulted in decreased p62 protein expression to levels comparable with the control group but increased LC3B II/I expression. These results suggested that treatment with CS@Lip@HKUST-1 could restore

autophagy in host cells infected with *H. pylori* in a PA-dependent manner (Fig. 4D and E).

We then conducted immunofluorescence staining of p62 and LC3B to further verify the above results. CLSM images showed enhanced deposition of autophagy-associated p62 protein (red fluorescence) (Fig. 4F, Supporting Information Fig. S29), while LC3B protein levels decreased in infected cells (Fig. 4G, Supporting Information Fig. S30). These results implied that autophagy was inhibited in *H. pylori*-infected cells, aligning well with our above results. In contrast, p62 deposition decreased and LC3B increased in cells treated with CS@Lip@HKUST-1 nanoparticles but not in the CS@Lip@HKUST-1 (No PA) group or untreated controls, suggesting that autophagy was rescued in the presence of PA. To further explore how CS@Lip@HKUST-1 promotes autophagy to induce host clearance of intracellular *H. pylori*, we performed lysosomal acidification and lysosomal calcium ion detection assays. As shown in Fig. 4H and Supporting Information Fig. S31, the intracellular lysosomal pH increased, as did calcium ion deposition in the lysosome (Fig. 4I) in *H. pylori*-infected cells.

Taken together, our results suggested that *H. pylori* could evade clearance from host cells by blocking lysosomal acidification through inhibition of calcium efflux from the lysosome to prevent the initiation of autophagy^{28,30}. In contrast, CS@Lip@HKUST-1 could promote the host elimination of intracellular *H. pylori* by activating lysosomal calcium efflux and acidification and restoring autophagy³⁸.

3.6. Anti-*H. pylori* activity of CS@Lip@HKUST-1 *in vivo*

Next, whether CS@Lip@HKUST-1 conferred the same effects on *H. pylori* clearance *in vivo* was examined. To this end, C57BL/6 mice were randomly divided into five *H. pylori*-infected groups (PBS, Lip@HKUST-1, CS@Lip@HKUST-1, antibiotics, and AP@CS@Lip@HKUST-1) and one uninfected control group (treated with PBS) (Fig. 5A). Each group was gavaged 1×10^8 colony-forming units (CFU)/mL *H. pylori* PMSS1 (or PBS for the uninfected control group) every other day for seven total inoculations. After four weeks of infection, five mice were randomly selected for sacrifice, and rapid urease tests, plate coating, and H&E staining were performed to assess the successful establishment of the *H. pylori*-infected mouse model. Compared to those of the control group (mice without *H. pylori* infection), the plates coated with stomach tissue from *H. pylori*-infected mice exhibited numerous small colonies (Supporting Information Fig. S32A), the rapid urease test showed a positive result (pink color) (Fig. S32B), and H&E staining revealed significant infiltration of inflammatory cells in the gastric tissues of *H. pylori*-infected mice, with a large number of rod-shaped bacteria observed on the surface of the gastric epithelium and in the gastric pits (Fig. S32C). These results indicate the successful establishment of our *H. pylori*-infected mouse model. We then administered the treatments immediately every other day for another two weeks, and the mice were sacrificed on the second day after the treatments were completed. Colony counts showed that *H. pylori* infection was significantly lower in the Lip@HKUST-1 group compared to PBS controls ($P < 0.05$), while the CS@Lip@HKUST-1 group had lower CFUs, comparable to antibiotic-treated positive controls, and the least infection was detected in mice treated with AP@CS@Lip@HKUST-1 ($P < 0.001$), which also had significantly fewer CFUs than the antibiotic treatment ($P < 0.05$) (Fig. 5B and C). The same trend was recapitulated in the urease activity test and rapid urease tests (Fig. 5D and E).

Additionally, H&E staining of stomach sections to evaluate gastric mucosal conditions revealed mucosal necrosis, extensive infiltration by inflammatory cells, and abundant *H. pylori* cells (red arrow) in the gastric mucosa and near the small recesses in *H. pylori*-infected mice treated with PBS. Whereas a reduction in inflammation as well as a decrease in *H. pylori* was observed in mice treated with Lip@HKUST and CS@Lip@HKUST-1, *H. pylori* colonization was still observed in mice treated with antibiotics. In contrast, inflammatory sites were largely absent in the stomach of mice treated with AP@CS@Lip@HKUST-1, while the mucosa appeared repaired with no obvious colonization by *H. pylori* cells (Fig. 5F, Supporting Information Fig. S33). These results indicated that the hydrogel-based delivery of HKUST-1.

3.7. Anti-inflammatory and mucosal repair effects

After colonizing the gastric mucosa, *H. pylori* destroys gastric epithelial cells by secreting a variety of virulence factors, resulting in inflammation and gastritis in the stomach, which are the primary drivers of *H. pylori*-related GI diseases, such as gastric erosion, peptic ulcers, and even gastric cancer⁶⁴. Therefore, the simultaneous elimination of *H. pylori*, inhibition of gastric inflammation and promotion of gastric mucosal repair are clinically important for gastric cancer prevention. In this part, we analyzed the anti-inflammatory and mucosal repair ability of AP@CS@Lip@HKUST-1 (Fig. 6A). Cell migration plays a key role in gastric mucosal repair^{65,66}. According to Fig. 6B and Supporting Information Fig. S34, AP@CS@Lip@HKUST-1 could significantly promote the migration of gastric epithelial cells in a time-dependent manner, which suggested that the nanoparticles had the ability to promote mucosal repair *in vitro*. As shown in Fig. 6C, the stomachs of mice infected with *H. pylori* showed a redder appearance, which may be attributed to eosinophil infiltration caused by gastritis, while after AP@CS@Lip@HKUST-1 treatment, the stomachs of mice returned to their normal color, which was not significantly different from that of the control group. Next, we further explored the expression of inflammatory factors in the stomach of mice after AP@CS@Lip@HKUST-1 treatment, and the results showed that the expression of the inflammatory factors MPO, IL-1 β , IL-6, IL-2, and IL-12 was significantly reduced after treatment with Lip@HKUST-1, CS@Lip@HKUST-1, and antibiotics ($P < 0.05$), while the AP@CS@Lip@HKUST-1 group showed the lowest expression (Fig. 6D–F, Supporting Information Fig. S35). In addition, the AP@CS@Lip@HKUST-1 group also showed the highest expression level of the anti-inflammatory factor IL-10 ($P < 0.05$) (Fig. 6G). The immunohistochemical results similarly demonstrated the anti-inflammatory effect of AP@CS@Lip@HKUST-1 (Supporting Information Fig. S36). In this study, AP@CS@Lip@HKUST-1 had the best anti-inflammatory effect, which might be due to the targeting of AP to the site of inflammation, allowing the nanoparticles to target the site of inflammation for precise release of Cu²⁺, thus achieving antibacterial and anti-inflammatory effects. However, it is also possible that this could be caused by a decrease in *H. pylori*, and based on the results available in this study, it is not yet possible to clearly discern the main cause of the modulation of inflammation in the stomach. However, based on previous literature reporting the anti-inflammatory effect of copper ions⁶⁷ and the significant anti-inflammatory effect of our material group compared to antibiotics, we can still infer that Cu²⁺ did exert some anti-inflammatory effects in our study.

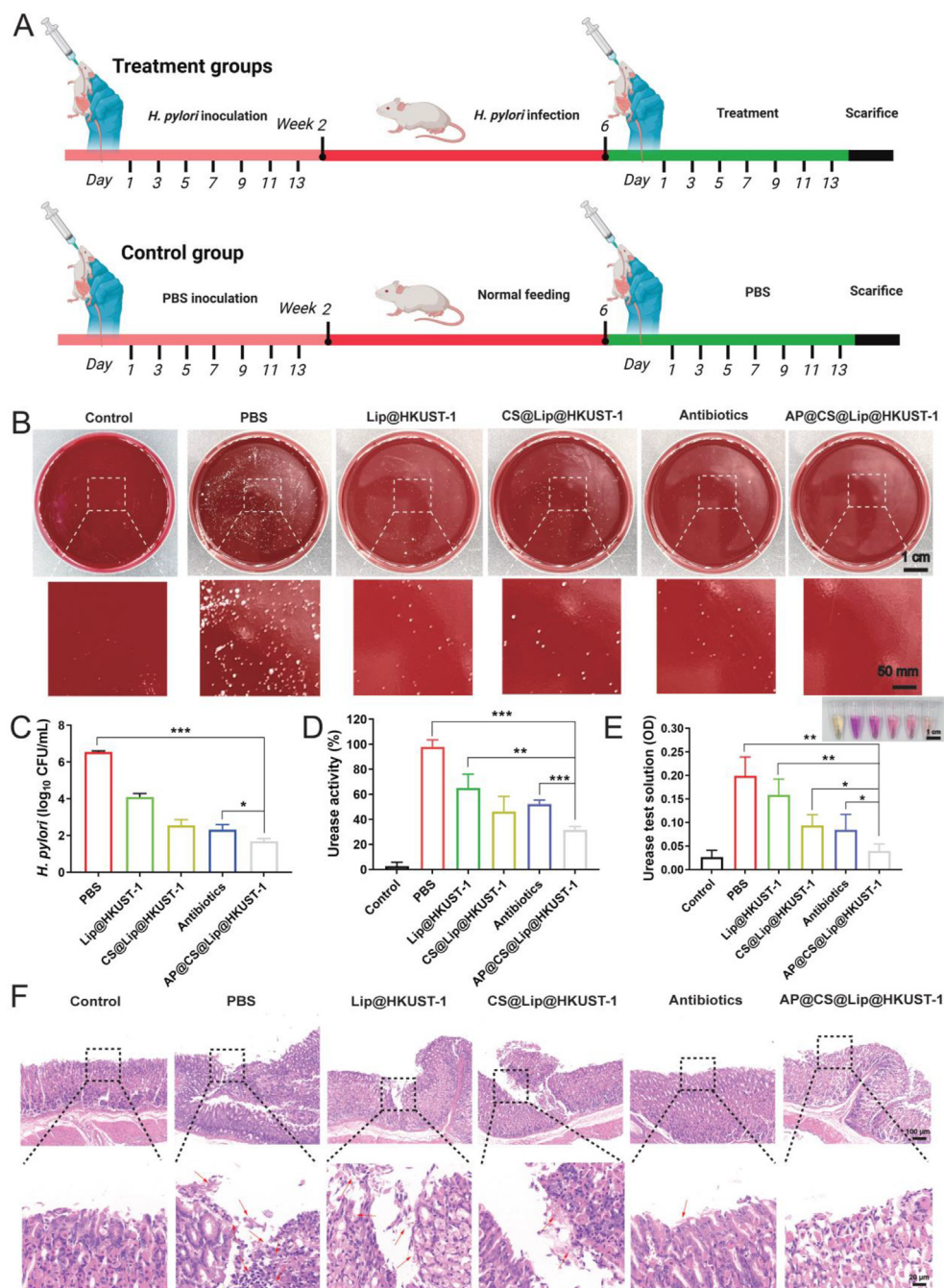


Figure 5 Antibacterial ability of nanoparticles and hydrogels. (A) Schematic diagram of the construction and treatment process for the *H. pylori*-infected mouse model. Colony plate images (B) and colony count plots (C) after different treatments in the *H. pylori*-infected mouse model. (D) Intra-gastric colonization of *H. pylori* after different treatments assessed by rapid urease assay. (E) The urease activity of *H. pylori* colonization in the stomach of mice after different treatments; scale: 1 cm. (F) H&E staining of gastric tissue from mice (red arrows represent *H. pylori*) after different treatments, scale: 100 μ m, enlarged figure scale: 20 μ m. Data are presented as the mean \pm SD ($n = 3$), * $P < 0.05$, ** $P < 0.01$, *** $P < 0.001$, **** $P < 0.0001$. ns, not significant.

After being infected with *H. pylori*, *H. pylori* secretes virulence factors, such as VacA and CagA, which could impair cell-cell junctions and cause their disruption, which is one of the main mechanisms of gastric mucosal damage caused by *H. pylori*⁶⁸. β -Catenin is a member of the armadillo protein family and can reflect the level of adhesion junctions of gastric epithelial cells⁶⁸. Similar to Ki-67 and PCNA, β -catenin can also reflect the proliferation of gastric epithelial cells⁵⁹. When gastric epithelial

cells are infected by *H. pylori*, β -catenin expression is reduced due to the disruption of gastric epithelial cell adhesion junctions by *H. pylori*. According to Fig. 6H and Supporting Information Fig. S37, treatment with Lip@HKUST-1 and CS@Lip@HKUST-1 significantly increased the expression of Ki-67, β -catenin and PCNA, and the expression of Ki-67, β -catenin and PCNA was the highest in the AP@CS@Lip@HKUST-1 group. Zonula occludens-1 (ZO-1), occludin-1 and claudin are tight junction proteins of

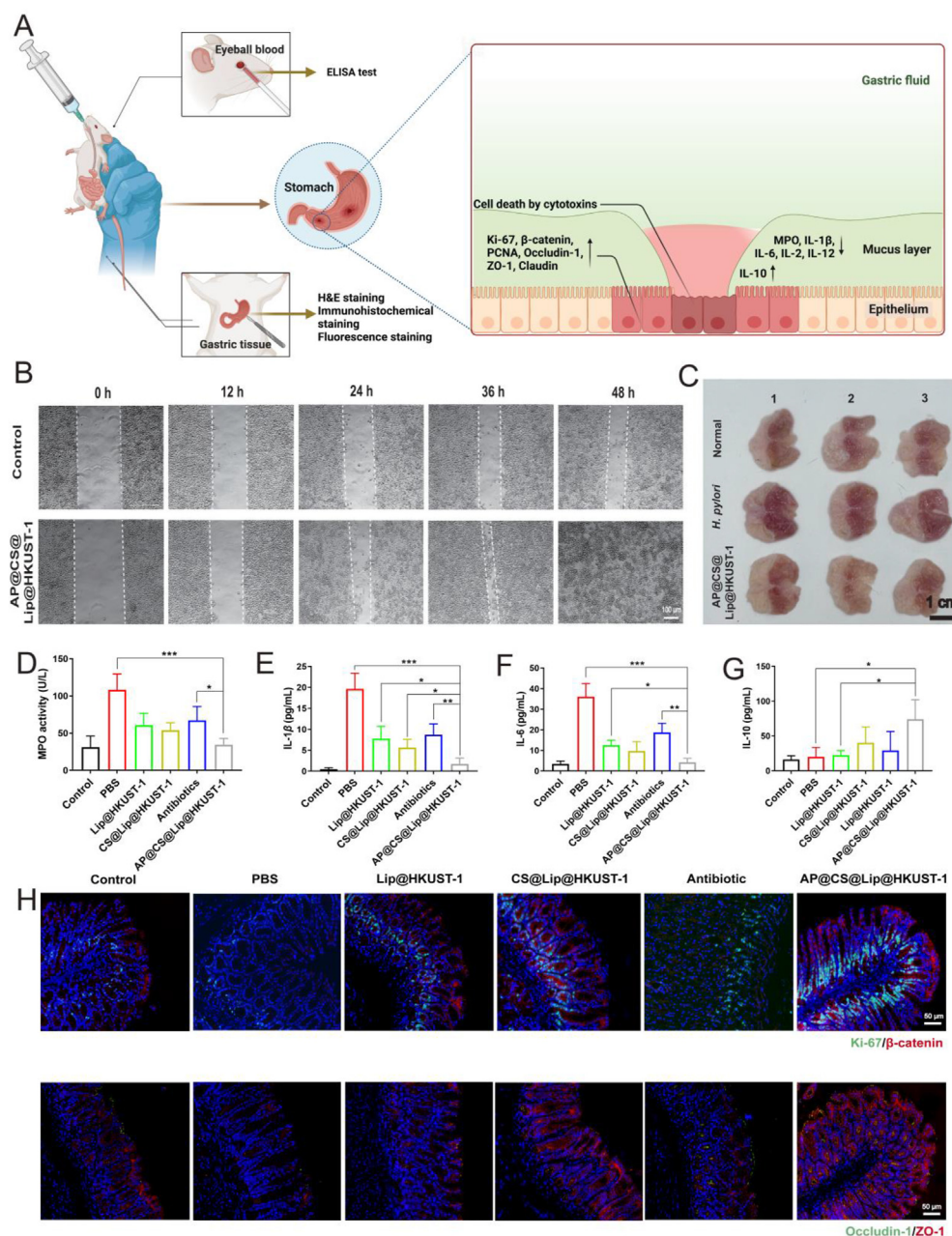


Figure 6 Anti-inflammatory and gastric mucosa repair ability of nanoparticles and hydrogels. (A) Schematic diagram of the anti-inflammatory and gastric mucosa repair ability of AP@CS@Lip@HKUST-1 in mice. (B) Cell migration after AP@CS@Lip@HKUST-1 treatment; scale: 100 μ m. (C) Gastric mucosa optical images of normal mice, *H. pylori*-infected mice, and *H. pylori*-infected mice after AP@CS@Lip@HKUST-1 treatment. The levels of (D) MPO activity, pro-inflammatory factors (E) IL-1 β , (F) IL-6, and anti-inflammatory factors (G) IL-10 in the serum of mice after different treatments were measured by ELISA. Data are presented as the mean \pm SD ($n = 3$), * $P < 0.05$, ** $P < 0.01$, *** $P < 0.001$, **** $P < 0.0001$. ns, not significant. (H) Fluorescence staining of gastric epithelial cells after different treatment in mice. The apoptosis of gastric epithelial cells was evaluated by Ki-67 and β -catenin fluorescence staining of gastric tissues; gastric mucosal epithelial repair in mice was evaluated by Occludin-1 and ZO-1 fluorescence staining of gastric tissues. Scale: 50 μ m.

gastric epithelial cells that can reflect gastric mucosal repair ability⁶⁸. As shown in Fig. 6H and Fig. S37, the expression of ZO-1, Occludin-1 and Claudin was very low in the *H. pylori* group, while the expression of ZO-1, Occludin-1 and Claudin was significantly increased after treatment with Lip@HKUST-1 and CS@Lip@HKUST-1, while AP@CS@Lip@HKUST-1 induced the highest expression of ZO-1 and Occludin-1 (Fig. 6H,

Fig. S37). All these results indicated that AP@CS@Lip@HKUST-1 has the best gastric mucosa repair effect.

Collectively, through the slow release of Cu²⁺, CS@Lip@HKUST-1 can not only kill *H. pylori* and relieve inflammation but also promote gastric mucosal repair by promoting cell proliferation as well as repairing gastric epithelial cell tight and adhesion junctions.

3.8. *In vivo* safety analysis and influence on the homeostasis of intestinal flora

Nanotoxicity *in vivo* should also be considered before further application of AP@CS@Lip@HKUST-1. Routine tests of blood (Supporting Information Fig. S38) and blood biochemistry (Supporting Information Fig. S39) in mice treated with AP@CS@Lip@HKUST-1 were close to those of the control group, with no abnormal blood parameters. In addition, no pathological symptoms were observed in sections of the heart, liver, spleen, lung or kidney of treated mice compared with the control group, indicating that the nanoparticles caused no pathological damage to the main organs (Supporting Information Fig. S40). These results suggested that the AP@CS@Lip@HKUST-1 hydrogel exhibited reasonable biocompatibility/low cytotoxicity *in vivo*.

In addition to good *in vivo* biocompatibility, negligible effects on the homeostasis of intestinal flora should be another goal when designing biomaterials for *H. pylori* eradication⁹. As shown in Fig. 7A and B, there was no significant difference in intestinal flora α -diversity (Chao 1 and Shannon indexes) between the AP@CS@Lip@HKUST-1 group and the control group (Supporting Information Table S1). However, in the antibiotic group, the intestinal bacterial richness was significantly reduced (Supporting Information Table S2). Next, we analyzed the relative abundance

of the intestinal flora colony structure. As shown in Fig. 7C, antibiotic treatment significantly increased harmful bacteria (*Escherichia-Shigella*) in the intestinal flora of mice, while no harmful bacteria were observed in the intestinal flora composition after AP@CS@Lip@HKUST-1 treatment. Additionally, we investigated the changes in the abundance of *Lactobacillus* and *Bifidobacterium* in the mouse intestine after AP@CS@Lip@HKUST-1 treatment (Supporting Information Fig. S41). The results showed that, compared to that in the control group, there was no significant change in the abundance of these two bacterial groups after AP@CS@Lip@HKUST-1 treatment. In contrast, the abundance of both bacterial groups significantly decreased after antibiotic treatment, further demonstrating that AP@CS@Lip@HKUST-1 treatment has a minimal effect on the intestinal flora. This may be due to the targeting of nanoparticles to the site of inflammation in the stomach as well as to *H. pylori*, resulting in their action only at the site of *H. pylori* colonization and greatly reducing the harm to the intestinal commensal flora^{59,69}. In addition, we also predicted changes in the intestinal flora after AP@CS@Lip@HKUST-1 treatment. As shown in Supporting Information Fig. S42, the function of intestinal flora after AP@CS@Lip@HKUST-1 treatment tended to promote cell proliferation metabolism, demonstrating that AP@CS@Lip@HKUST-1 could promote mucosal repair.

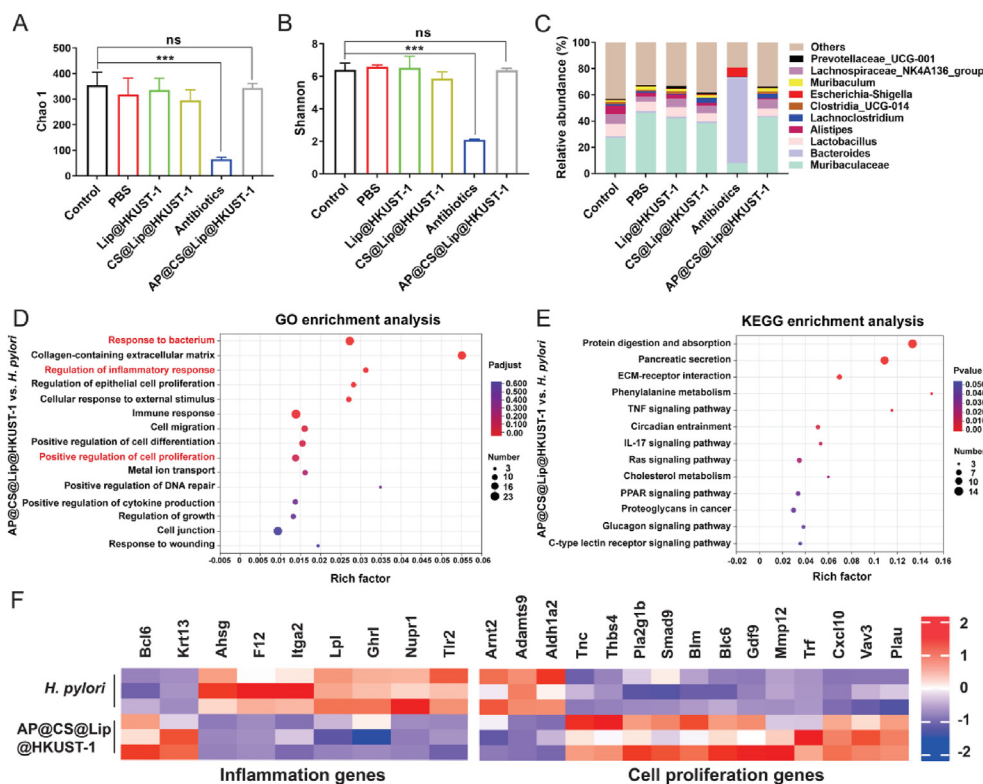


Figure 7 The impact of AP@CS@Lip@HKUST-1 on the homeostasis of intestinal microbiota and transcriptome analysis of the stomach after AP@CS@Lip@HKUST-1 treatment. Flora richness (A) Chao 1 diversity and (B) Shannon indexes of α -diversity in the feces of mice after different treatments. (C) Relative abundance of colony structures in mouse feces after treatment was measured by 16S rRNA sequencing. (D) Bubble diagram showing GO pathway enrichment analysis of AP@CS@Lip@HKUST-1/*H. pylori* comparison. (E) Bubble diagram showing KEGG pathway enrichment analysis of AP@CS@Lip@HKUST-1/*H. pylori* comparison. (F) Gene expression analysis of the positive regulation of the inflammatory response and cell proliferation in mouse gastric tissue between the AP@CS@Lip@HKUST-1 treatment and *H. pylori* (PBS treatment) groups, $n = 3$ mice per treatment. Data are presented as the mean \pm SD ($n = 3$). * $P < 0.05$, ** $P < 0.01$, *** $P < 0.001$, **** $P < 0.0001$. ns, not significant.

Overall, the results of the *in vivo* safety evaluation and microbiome analysis showed that AP@CS@Lip@HKUST-1 has a favorable *in vivo* safety profile, with minimal impact on the intestinal flora while eradicating *H. pylori*.

3.9. Role of AP@CS@Lip@HKUST-1 in the stomach by transcriptomic analysis

To further investigate the molecular mechanisms underlying the efficacy of AP@CS@Lip@HKUST-1 treatment, we collected gastric tissues from control mice as well as *H. pylori* mice and mice after gavage treatment for transcriptomic analysis (Supporting Information Fig. S43). In total, 3276 significantly differentially expressed genes (DEGs) were found to be expressed ($|\log_2 \text{FC}| \geq 1$, q -value < 0.05), and the Venn plot showed in detail the genetic changes between the three groups (Supporting Information Fig. S44). Compared with the *H. pylori* group, the AP@CS@Lip@HKUST-1 group exhibited 278 upregulated genes and 162 downregulated genes among 440 DEGs, and the volcano plot shows the distribution of these DEGs (Supporting Information Fig. S45). Then, GO functional enrichment analysis was performed to elucidate the pathways in which the DEGs were involved. As shown in Fig. 7D, the GO functional enrichment analysis proved that the pathways activated by AP@CS@Lip@HKUST-1 treatment were correlated with those affected by bacterial infection, which confirmed the antibacterial function of our nanoparticles. In addition, GO enrichment analysis also showed that DEGs were associated with inflammatory responses and positive cell proliferation, which was also consistent with our previous experimental results, validating the efficacy of our nanoparticles in promoting cell proliferation and gastric mucosal repair as well as anti-inflammatory properties. Moreover, KEGG pathway analysis also revealed that DEGs in the AP@CS@Lip@HKUST-1 group were enriched in inflammation-related pathways, including TNF signaling pathways and IL-17 signaling pathways, and cell proliferation-related pathways, including ECM-receptor interaction signaling pathways, Ras signaling pathways and PPAR signaling pathways, suggesting that AP@CS@Lip@HKUST-1 may exert anti-inflammatory and pro-repair functions (Fig. 7E). Furthermore, we analyzed the DEGs in the GO analysis in the inflammatory response as well as cell proliferation between the AP@CS@Lip@HKUST-1 and *H. pylori* groups. As shown in Fig. 7F, *H. pylori* infection significantly suppressed the expression of anti-inflammatory genes (*Bcl6* and *Krt13*) while leading to the upregulation of proinflammatory gene (e.g., *Itga2* and *Lpl*) expression, and AP@CS@Lip@HKUST-1 treatment resulted in the downregulation of these proinflammatory genes and the upregulation of anti-inflammatory gene expression, demonstrating the anti-inflammatory efficacy of AP@CS@Lip@HKUST-1. In addition, our results also found that genes related to the promotion of cell proliferation (e.g., *Tnc*, *Blm*, *Mmp12*) were also upregulated after AP@CS@Lip@HKUST-1 treatment, suggesting that AP@CS@Lip@HKUST-1 has a repairing effect on gastric mucosa (Fig. 7F). In addition, RT-qPCR also demonstrated the above results (Supporting Information Fig. S46). Taken together, these results indicate that AP@CS@Lip@HKUST-1 showed anti-inflammatory and proliferative effects by increasing the expression of a series of genes associated with anti-inflammation and cell proliferation.

To the best of our knowledge, this is the first multifunctional antibiotic-free platform that simultaneously eradicates planktonic, biofilm, and intracellular *H. pylori* without disrupting the

homeostasis of the intestinal flora while also repairing the gastric mucosa. Simultaneous eradication of planktonic, biofilm, and intracellular *H. pylori* can kill *H. pylori* more thoroughly, and the repair of the gastric mucosa can once again establish a complete gastric mucosal barrier to prevent the body from being infected with *H. pylori* again.

4. Conclusions

This study introduces a multi-effect Cu^{2+} -organic nanoparticle platform for clearing planktonic, biofilm-sequestered, and intracellular *H. pylori* in the stomach. Sequential coatings of these nanoparticles also alleviate inflammation while promoting the repair of the gastric mucosa without damaging the intestinal microecology. This platform, comprising HKUST-1 within an RHL/PA/CHOL liposomal membrane layer enveloped within chitosan (CS) and delivered as a negatively charged AP-based hydrogel, first enters the stomach and targets positively charged inflammation sites in the stomach. The hydrogel is subsequently hydrolyzed by secreted MMPs in the stomach environment, releasing CS@Lip@HKUST-1. These nanoparticles then adhere to *H. pylori* aggregates at inflammatory sites through electrostatic interactions between the cell membrane and CS. The slow release of Cu^{2+} from HKUST-1 disrupts the bacterial membrane and inhibits urease activity, resulting in cytotoxicity toward *H. pylori*. Additionally, the RHL component of the lipid membrane can disrupt *H. pylori* biofilms and prevent its reformation, while the PA component can activate autophagy in infected cells, facilitating clearance of intracellular *H. pylori*. In addition to its antibacterial effects, the gradual accumulation of Cu^{2+} confers anti-inflammatory effects and enhances the repair of damaged mucosa through previously reported positive effects on angiogenesis and collagen deposition. The findings in this study indicate that this antibiotic-free, multifunctional, HKUST-1-based platform and its Cu^{2+} -based mechanism of action may serve as an effective therapeutic option for recalcitrant *H. pylori* infection and warrant further exploration and development for clinical application.

Acknowledgments

This work was supported by the National Natural Science Foundation of China (No. 82072051), the Strategic Consulting Research Project of the Chinese Academy of Engineering (No. 2021-ZX-12, China), the Project of the Shanghai Municipal Health Commission (No. 2019SY001, China), the Shanghai Clinical Medical Research Center for Digestive Diseases Project (No. 19MC1910200, China), the Shanghai Outstanding Academic Leaders Program (No. 21XD14049, China), and the Nanchang University Graduate Student Innovation Fund (No. YC2023-B102, China).

Author contributions

Yongkang Lai: Writing—original draft, data curation, formal analysis, conceptualization, methodology. Tinglin Zhang: data curation, formal analysis, methodology. Xiaojing Yin: data curation, methodology, investigation. Chunping Zhu: methodology, validation. Yiqi Du: project administration, conceptualization, supervision, resources, funding acquisition. Zhaoshen Li: project administration, conceptualization, writing—review & editing, funding acquisition. Jie Gao: project administration, conceptualization, supervision, writing—review & editing.

Conflicts of interest

The authors declare no competing financial interests.

Appendix A. Supporting information

Supplementary information to this article can be found online at <https://doi.org/10.1016/j.apsb.2024.03.014>.

References

- Zhou XZ, Lyu NH, Zhu HY, Cai QC, Kong XY, Xie P, et al. Large-scale, national, family-based epidemiological study on *Helicobacter pylori* infection in China: the time to change practice for related disease prevention. *Gut* 2023;**72**:855–69.
- Malferteiner P, Megraud F, Rokkas T, Gisbert JP, Liou JM, Schulz C, et al. Management of *Helicobacter pylori* infection: the Maastricht VI/Florence consensus report. *Gut* 2022;**71**:1724–62.
- Hooi JKY, Lai WY, Ng WK, Suen MMY, Underwood FE, Tanyingoh D, et al. Global prevalence of *Helicobacter pylori* infection: systematic review and meta-analysis. *Gastroenterology* 2017;**153**:420–9.
- Li Y, Choi H, Leung K, Jiang F, Graham DY, Leung WK. Global prevalence of *Helicobacter pylori* infection between 1980 and 2022: a systematic review and meta-analysis. *Lancet Gastroenterol Hepatol* 2023;**8**:553–64.
- Ding SZ, Du YQ, Lu H, Wang WH, Cheng H, Chen SY, et al. Chinese consensus report on family-based *Helicobacter pylori* infection control and management (2021 edition). *Gut* 2022;**71**:238–53.
- Baj J, Forma A, Sitarz M, Portincasa P, Garruti G, Krasowska D, et al. *Helicobacter pylori* virulence factors-mechanisms of bacterial pathogenicity in the gastric microenvironment. *Cells* 2020;**10**:27.
- Lee YC, Chiang TH, Chou CK, Tu YK, Liao WC, Wu MS, et al. Association between *Helicobacter pylori* eradication and gastric cancer incidence: a systematic review and meta-analysis. *Gastroenterology* 2016;**150**:1113. 24.e1115.
- Liou JM, Malferteiner P, Lee YC, Sheu BS, Sugano K, Cheng HC, et al. Screening and eradication of *Helicobacter pylori* for gastric cancer prevention: the taipei global consensus. *Gut* 2020;**69**:2093–112.
- Lai YK, Wei W, Du YQ, Gao J, Li ZS. Biomaterials for *Helicobacter pylori* therapy: therapeutic potential and future perspectives. *Gut Microb* 2022;**14**:2120747.
- Polk DB, Peek Jr RM. *Helicobacter pylori*: gastric cancer and beyond. *Nat Rev Cancer* 2010;**10**:403–14.
- Raju D, Hussey S, Ang M, Terebiznik MR, Sibony M, Galindo-Mata E, et al. Vacuolating cytotoxin and variants in atg1611 that disrupt autophagy promote *Helicobacter pylori* infection in humans. *Gastroenterology* 2012;**142**:1160–71.
- Du YQ, Zhu HY, Liu J, Li JN, Chang X, Zhou LY, et al. Consensus on eradication of *Helicobacter pylori* and prevention and control of gastric cancer in China (2019, Shanghai). *J Gastroenterol Hepatol* 2020;**35**:624–9.
- Ford AC, Forman D, Hunt RH, Yuan Y, Moayyedi P. *Helicobacter pylori* eradication therapy to prevent gastric cancer in healthy asymptomatic infected individuals: systematic review and meta-analysis of randomised controlled trials. *Br Med J* 2014;**348**:g3174.
- Cai QC, Zhu CP, Yuan Y, Feng Q, Feng YC, Hao YX, et al. Development and validation of a prediction rule for estimating gastric cancer risk in the Chinese high-risk population: a nationwide multi-centre study. *Gut* 2019;**68**:1576–87.
- Palrasu M, Zaika E, El-Rifai W, Garcia-Buitrago M, Piazzuelo MB, Wilson KT, et al. Bacterial caga protein compromises tumor suppressor mechanisms in gastric epithelial cells. *J Clin Invest* 2020;**130**:2422–34.
- Cao LL, Zhu SM, Lu H, Soutto M, Bhat N, Chen Z, et al. *Helicobacter pylori*-induced rasal2 through activation of nuclear factor- κ b promotes gastric tumorigenesis via β -catenin signaling axis. *Gastroenterology* 2022;**162**:1716–31.e17.
- Choi IJ, Kim CG, Lee JY, Kim YI, Kook MC, Park B, et al. Family history of gastric cancer and *Helicobacter pylori* treatment. *N Engl J Med* 2020;**382**:427–36.
- Chiang TH, Chang WJ, Chen SL, Yen AM, Fann JC, Chiu SY, et al. Mass eradication of *Helicobacter pylori* to reduce gastric cancer incidence and mortality: a long-term cohort study on matsu islands. *Gut* 2021;**70**:243–50.
- Yan LJ, Chen Y, Chen F, Tao T, Hu ZJ, Wang JZ, et al. Effect of *Helicobacter pylori* eradication on gastric cancer prevention: updated report from a randomized controlled trial with 26.5 years of follow-up. *Gastroenterology* 2022;**163**:154–62.e3.
- Ford AC, Yuan Y, Moayyedi P. Long-term impact of *Helicobacter pylori* eradication therapy on gastric cancer incidence and mortality in healthy infected individuals: a meta-analysis beyond 10 years of follow-up. *Gastroenterology* 2022;**163**:754–56.e1.
- Yang L, Kartsonaki C, Yao P, de Martel C, Plummer M, Chapman D, et al. The relative and attributable risks of cardia and non-cardia gastric cancer associated with *Helicobacter pylori* infection in China: a case-cohort study. *Lancet Public Health* 2021;**6**:e888–96.
- Boltin D, Ben-Zvi H, Perets TT, Kamenetsky Z, Samra Z, Dickman R, et al. Trends in secondary antibiotic resistance of *Helicobacter pylori* from 2007 to 2014: has the tide turned?. *J Clin Microbiol* 2015;**53**:522–7.
- Tshibangu-Kabamba E, Yamaoka Y. *Helicobacter pylori* infection and antibiotic resistance — from biology to clinical implications. *Nat Rev Gastroenterol Hepatol* 2021;**18**:613–29.
- Thung I, Aramin H, Vavinskaya V, Gupta S, Park JY, Crowe SE, et al. Review article: the global emergence of *Helicobacter pylori* antibiotic resistance. *Aliment Pharmacol Ther* 2016;**43**:514–33.
- Hu W, Zhang L, Li MX, Shen J, Liu XD, Xiao ZG, et al. Vitamin d3 activates the autolysosomal degradation function against *Helicobacter pylori* through the pdia3 receptor in gastric epithelial cells. *Autophagy* 2019;**15**:707–25.
- Yang YH, Shu X, Xie C. An overview of autophagy in *Helicobacter pylori* infection and related gastric cancer. *Front Cell Infect Microbiol* 2022;**12**:847716.
- Xie C, Li NS, Wang H, He C, Hu Y, Peng C, et al. Inhibition of autophagy aggravates DNA damage response and gastric tumorigenesis via rad51 ubiquitination in response to *Helicobacter pylori* infection. *Gut Microb* 2020;**11**:1567–89.
- Zou YQ, Chen XN, Sun YY, Li PY, Xu M, Fang PC, et al. Antibiotics-free nanoparticles eradicate *Helicobacter pylori* biofilms and intracellular bacteria. *J Control Release* 2022;**348**:370–85.
- Hathroubi S, Servetas SL, Windham I, Merrell DS, Ottemann KM. *Helicobacter pylori* biofilm formation and its potential role in pathogenesis. *Microbiol Mol Biol Rev* 2018;**82**: e00001-18.
- Chen XN, Zou YQ, Zhang SQ, Fang PC, Li SX, Li PY, et al. Multifunctional vesicles improve *Helicobacter pylori* eradication by a comprehensive strategy based on complex pathological microenvironment. *Acta Pharm Sin B* 2022;**12**:3498–512.
- Qiao YQ, Ma Y, Tong Y, Liu WT, Wang S, Zheng Y, et al. Phototherapy and mechanism exploration of biofilm and multidrug-resistant *Helicobacter pylori* by bacteria-targeted nir photosensitizer. *Small* 2023;**19**:e2205248.
- Xiao J, Zhu Y, Huddleston S, Li P, Xiao B, Farha OK, et al. Copper metal-organic framework nanoparticles stabilized with folic acid improve wound healing in diabetes. *ACS Nano* 2018;**12**:1023–32.
- Liang YT, Yao Y, Liu Y, Li YM, Xu CH, Fu LH, et al. Curcumin-loaded hkust-1@ carboxymethyl starch-based composites with moisture-responsive release properties and synergistic antibacterial effect for perishable fruits. *Int J Biol Macromol* 2022;**214**:181–91.
- Kiran GS, Ninawe AS, Lipton AN, Pandian V, Selvin J. Rhamnolipid biosurfactants: evolutionary implications, applications and future prospects from untapped marine resource. *Crit Rev Biotechnol* 2016;**36**:399–415.

35. Li PY, Chen XN, Shen YN, Li HT, Zou YQ, Yuan G, et al. Mucus penetration enhanced lipid polymer nanoparticles improve the eradication rate of *Helicobacter pylori* biofilm. *J Control Release* 2019; **300**:52–63.
36. Steinberg BE, Grinstein S. Pathogen destruction versus intracellular survival: the role of lipids as phagosomal fate determinants. *J Clin Invest* 2008; **118**:2002–11.
37. Yeung T, Grinstein S. Lipid signaling and the modulation of surface charge during phagocytosis. *Immunol Rev* 2007; **219**:17–36.
38. Greco E, Quintiliani G, Santucci MB, Serafino A, Ciccaglione AR, Marcantonio C, et al. Janus-faced liposomes enhance antimicrobial innate immune response in mycobacterium tuberculosis infection. *Proc Natl Acad Sci U S A* 2012; **109**:E1360–8.
39. Balboa MA, de Pablo N, Meana C, Balsinde J. The role of lipins in innate immunity and inflammation. *Biochim Biophys Acta Mol Cell Biol Lipids* 2019; **1864**:1328–37.
40. Aghbashlo M, Amiri H, Moosavi Basri SM, Rastegari H, Lam SS, Pan J, et al. Tuning chitosan's chemical structure for enhanced biological functions. *Trends Biotechnol* 2023; **41**:785–97.
41. Rahayu DP, De Mori A, Yusuf R, Draheim R, Lalatsa A, Roldo M. Enhancing the antibacterial effect of chitosan to combat orthopaedic implant-associated infections. *Carbohydr Polym* 2022; **289**:119385.
42. Luo DQ, Guo JH, Wang FJ, Sun J, Li GW, Cheng XL, et al. Preparation and evaluation of anti-*Helicobacter pylori* efficacy of chitosan nanoparticles *in vitro* and *in vivo*. *J Biomater Sci Polym Ed* 2009; **20**:1587–96.
43. Lin YH, Chang CH, Wu YS, Hsu YM, Chiou SF, Chen YJ. Development of pH-responsive chitosan/heparin nanoparticles for stomach-specific anti-*Helicobacter pylori* therapy. *Biomaterials* 2009; **30**:3332–42.
44. Jing ZW, Jia YY, Wan N, Luo M, Huan ML, Kang TB, et al. Design and evaluation of novel pH-sensitive ureido-conjugated chitosan/tpp nanoparticles targeted to *Helicobacter pylori*. *Biomaterials* 2016; **84**:276–85.
45. Zhang S, Ermann J, Succi MD, Zhou A, Hamilton MJ, Cao B, et al. An inflammation-targeting hydrogel for local drug delivery in inflammatory bowel disease. *Sci Transl Med* 2015; **7**:300ra128.
46. Bamidele OP, Duodu KG, Emmambux MN. Encapsulation and antioxidant activity of ascorbyl palmitate with maize starch during pasting. *Carbohydr Polym* 2017; **166**:202–8.
47. Borkow G, Gabbay J, Dardik R, Eidelman AI, Lavie Y, Grunfeld Y, et al. Molecular mechanisms of enhanced wound healing by copper oxide-impregnated dressings. *Wound Repair Regen* 2010; **18**:266–75.
48. Sen CK, Khanna S, Venojarvi M, Trikha P, Ellison EC, Hunt TK, et al. Copper-induced vascular endothelial growth factor expression and wound healing. *Am J Physiol Heart Circ Physiol* 2002; **282**:H1821–7.
49. Kornblatt AP, Nicoletti VG, Travaglia A. The neglected role of copper ions in wound healing. *J Inorg Biochem* 2016; **161**:1–8.
50. Xiao J, Chen S, Yi J, Zhang H, Ameer GA. A cooperative copper metal-organic framework-hydrogel system improves wound healing in diabetes. *Adv Funct Mater* 2017; **27**:1604872.
51. Behrens B, Engelen J, Tiso T, Blank LM, Hayen H. Characterization of rhamnolipids by liquid chromatography/mass spectrometry after solid-phase extraction. *Anal Bioanal Chem* 2016; **408**:2505–14.
52. Liu S, Liu X, Ren YH, Wang PH, Pu YJ, Yang R, et al. Mussel-inspired dual-cross-linking hyaluronic acid/e-polylysine hydrogel with self-healing and antibacterial properties for wound healing. *ACS Appl Mater Interfaces* 2020; **12**:27876–88.
53. Czerwińska-Główka D, Krukiewicz K. Guidelines for a morphometric analysis of prokaryotic and eukaryotic cells by scanning electron microscopy. *Cells* 2021; **10**:3304.
54. Li NS, Xu XB, Zhan Y, Fei X, Ouyang YB, Zheng P, et al. Yap and β -catenin cooperate to drive h. Pylori-induced gastric tumorigenesis. *Gut Microb* 2023; **15**:2192501.
55. Andrew A, Wyatt JI, Dixon MF. Observer variation in the assessment of chronic gastritis according to the Sydney system. *Histopathology* 1994; **25**:317–22.
56. Han S, Ciufo RA, Meyerson ML, Keitz BK, Mullins CB. Solvent-free vacuum growth of oriented hkust-1 thin films. *J Mater Chem A* 2019; **7**:19396–406.
57. Loera-Serna S, Oliver-Tolentino MA, de Lourdes López-Núñez M, Santana-Cruz A, Guzmán-Vargas A, Cabrera-Sierra R, et al. Electrochemical behavior of [Cu₃(BTC)₂] metal-organic framework: the effect of the method of synthesis. *J Alloys Compd* 2012; **540**:113–20.
58. Du JC, Zhou CL, Yang ZJ, Cheng J, Shen YY, Zeng XJ, et al. Conversion of solid Cu₂(OH)₂CO₃ into HKUST-1 metal-organic frameworks: toward an under-liquid superamphiphobic surface. *Surf Coat Technol* 2019; **363**:282–90.
59. Zhang W, Zhou YA, Fan YT, Cao R, Xu YY, Weng ZZ, et al. Metal-organic-framework-based hydrogen-release platform for multi-effective *Helicobacter pylori* targeting therapy and intestinal flora protective capabilities. *Adv Mater* 2022; **34**:e2105738.
60. Xie XH, Jin X, He BB, Zou Y, Yang JM, Liu CJ, et al. A change-prone zwitterionic hyperbranched terpolymer-based diabetic wound dressing. *Appl Mater Today* 2022; **27**:101477.
61. Yang SJ, Huang CH, Yang JC, Wang CH, Shieh MJ. Residence time-extended nanoparticles by magnetic field improve the eradication efficiency of *Helicobacter pylori*. *ACS Appl Mater Interfaces* 2020; **12**:54316–27.
62. Lin YH, Tsai SC, Lai CH, Lee CH, He ZS, Tseng GC. Genipin-cross-linked fucose-chitosan/heparin nanoparticles for the eradication of *Helicobacter pylori*. *Biomaterials* 2013; **34**:4466–79.
63. Xia X, Yin ZW, Yang YX, Li SK, Wang LL, Cai XQ, et al. In situ upregulating heat shock protein 70 via gastric nano-heaters for the interference of *Helicobacter pylori* infection. *ACS Nano* 2022; **16**:14043–54.
64. Sugano K, Tack J, Kuipers EJ, Graham DY, El-Omar EM, Miura S, et al. Kyoto global consensus report on *Helicobacter pylori* gastritis. *Gut* 2015; **64**:1353–67.
65. Kim YW, Lee WH, Choi SM, Seo YY, Ahn BO, Kim SH, et al. DA6034 promotes gastric epithelial cell migration and wound-healing through the mtor pathway. *J Gastroenterol Hepatol* 2012; **27**:397–405.
66. Teal E, Dua-Awreh M, Hirshorn ST, Zavros Y. Role of metaplasia during gastric regeneration. *Am J Physiol Cell Physiol* 2020; **319**:C947–54.
67. Solier S, Müller S, Cañeque T, Versini A, Mansart A, Sindikubwabo F, et al. A druggable copper-signalling pathway that drives inflammation. *Nature* 2023; **617**:386–94.
68. Prashar A, Capurro ML, Jones NL. Under the radar: strategies used by *Helicobacter pylori* to evade host responses. *Annu Rev Physiol* 2022; **84**:485–506.
69. Yu J, Guo Z, Yan J, Bu C, Peng C, Li C, et al. Gastric acid-responsive ROS nanogenerators for effective treatment of *Helicobacter pylori* infection without disrupting homeostasis of intestinal flora. *Adv Sci* 2023; **e2206957**.